Title

Hybrid simulation theory for a crane structure

Permalink

https://escholarship.org/uc/item/51w1s68z

Authors

Govindjee, Sanjay
Drazin, Paul

Publication Date

2017-02-01

Report No.
UCB/SEMM-2017/01

Structural Engineering
Mechanics and Materials

Hybrid Simulation Theory for a Crane Structure

By

Paul L. Drazin and Sanjay Govindjee

February 2017

Department of Civil and Environmental Engineering
University of California, Berkeley

UCB/SEMM-2017/01

HYBRID SIMULATION THEORY FOR A CRANE STRUCTURE

Paul L. Drazin[1], Sanjay Govindjee[2]

Abstract

Hybrid simulation is a simulation technique which allows one to study the time evolution of a system by physically testing a subset of it while the remainder is represented by a numerical model that is attached to the physical portion by sensors and actuators. This technique allows one to study a large or complicated mechanical system while only requiring a subset of the complete system to actually be present in a laboratory. The errors that arise from the use of sensors and actuators, however, requires careful attention, if a valid simulation is to be guaranteed. Prior efforts to understand the theoretical behavior of hybrid simulation have involved linear systems with constant errors or simple one degree of freedom systems. Missing is a theoretical investigation of the behavior of hybrid simulation for larger multi-degree of freedom nonlinear systems.

In this paper, a model for hybrid simulation is applied to a crane structure. This system offers complex nonlinear characteristics, and multiple degrees of freedom comparable to what would be found in a standard hybrid simulation experiment. The setup of the hybrid system involves splitting the mechanical system into two or more substructures and using a model for an actuator and controller at the interface of the two substructures to maintain the dynamical response. The error analysis of the hybrid system is through the use of L^2 norms on different aspects of the mechanical systems to provide a general overview on the multiple effects that can occur because of hybrid split.

It is found that the location of the hybrid split has a major impact on the results of a hybrid experiment. Also, based on the error metrics used in this paper, the location of the hybrid split affects the error in the hybrid system more than the quantity of hybrid splits. Finally, the resonant frequencies of the unforced system have significant influence on the error that a hybrid test experiences and should be avoided if possible.

Keywords:
Hybrid simulation, Hybrid testing, Error analysis, Nonlinear dynamics, Frequency analysis

1. Introduction

Hybrid simulation (or hybrid-testing) is a simulation technique that has been around for nearly 30 years [1, 2] and has become quite popular among Civil Engineering laboratories, primarily for seismic testing [2, 3]. There has also been some limited application of hybrid simulation to other mechanical systems not directly related to Civil Engineering or seismic testing; see e.g. [4]. Hybrid simulation is still an active area of research, and is used quite extensively to determine the dynamic behavior of large or complicated structures [5, 6, 7, 8, 9]. The driving force behind hybrid simulation is the difficulty in experimentally testing large dynamical systems, especially those subject to earthquakes. The largest testing facility in world is the E-Defense facility [10] which can test structures with a 20m × 15m plan and 12MN weight. Even though this facility has a large capacity, it is limited to which systems can be tested, is expensive, has limited throughput, and does not easily allow for modifications. Due to the limitations of full-size experiments, hybrid simulation offers a cost effective alternative that can be used to give experimental results for aspects of a system that do not have working or validated computational models for all components.

The basic structure of hybrid simulation and its many variants [11] is to leverage the use of computational models to reduce the size of the physical system that needs to be present in a laboratory. In this way, aspects of the system

---

Email addresses: `pdrazin@berkeley.edu` (Paul L. Drazin), `s_g@berkeley.edu` (Sanjay Govindjee)

[1] Ph.D. Candidate, Dept. of Mechanical Engineering, College of Engineering, Univ. of California, Berkeley, Berkeley, CA 94720

[2] Prof., Dept. of Civil and Environmental Engineering, College of Engineering, Univ. of California, Berkeley, Berkeley, CA 94720

January 20, 2017

that have validated computational models can be simulated, where as other aspects that have complicated or unknown models are tested physically, while maintaining the dynamic fidelity of the entire system. The setup for the hybrid system assumes that the system of interest is separated at specific locations, and then actuators are used to drive the physical part in the laboratory, meanwhile, position and force feedback data from sensors are used as an input to the computational model. A simple schematic of this process is shown in Fig. 1.

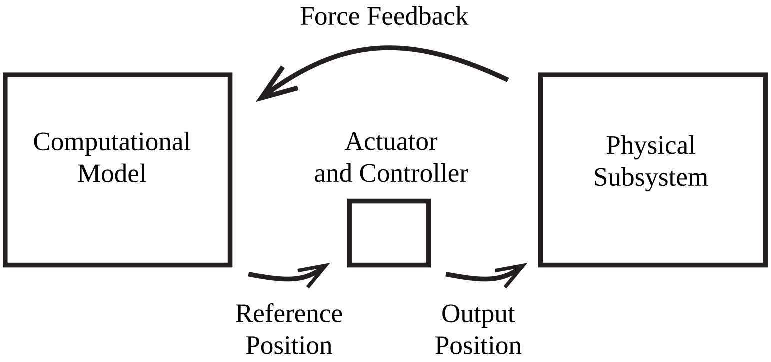

Figure 1: A simple diagram of a hybrid system setup.

Notwithstanding the fact that variants of hybrid simulation have been used in experimental mechanics for over 30 years, there has been a considerable lack of theoretical understanding of the true dynamics behind this experimental method. Most analyses of hybrid simulation are concerned with the errors related to time integrators and control systems, with the idea that improving those aspects of a hybrid simulation experiment, alone, will provide a more accurate representation of the physical reality [12, 13, 14]. However, there are bound to be errors in the dynamics of a hybrid system when compared to an equivalent reference system due to the introduction of sensors and actuators into the system, and there is limited knowledge concerning those errors. Some theoretical work has been conducted on Euler-Bernoulli beams, Kirchhoff-Love plates, and simple pendulums; see [15, 16, 17]. In these works, simple linear systems or single degree of freedom nonlinear systems were used to understand the errors that might occur during a hybrid simulation experiment. While [15, 16, 17] provide a good start in the process of understanding hybrid simulation errors, this paper aims to expand upon that understand by applying hybrid simulation to a more complicated nonlinear multi-degree of freedom system. Also, the three previous papers focused only on a hybrid split at a single location, where as this paper will look at the effects of how the location of the hybrid split affects errors, as well as multiple hybrid splits.

This paper focuses solely on the *theoretical* performance of hybrid simulation as an experimental method, ignoring all of the numerical and random errors, as this leads to a best case scenario for a hybrid experiment; see e.g. [3, 18]. This approach eliminates the errors associated with time integration methods and signal noise and focuses only on the errors that are generated by systematic interface mismatch errors – an element that is always present in hybrid simulations. In this paper, the actuator is modeled as a simple spring-mass-damper system and controlled by a PI controller. This setup for the hybrid system is similar to one used previously [17].

As a model problem, we focus upon a station boom crane. This system has direct applications to a potential hybrid simulation experiment, in that understanding the motion of a crane structure during an earthquake can be invaluable. However, experimentally testing a full crane structure is impractical. We aim to provide a framework for understanding how hybrid simulation affects the dynamical response of a given structure, even when that structure is quite complicated with many degrees of freedom.

2. General Theory of Hybrid Simulation

In this section we will set up a general frame work for thinking about hybrid simulation.

2.1. The Reference System

First, we need to set up the reference system to which the hybrid system will be compared. A mechanical system with domain $\mathcal{D}$ is considered, as shown in Fig. 2a. The mechanical response of the system is characterized by a state vector,

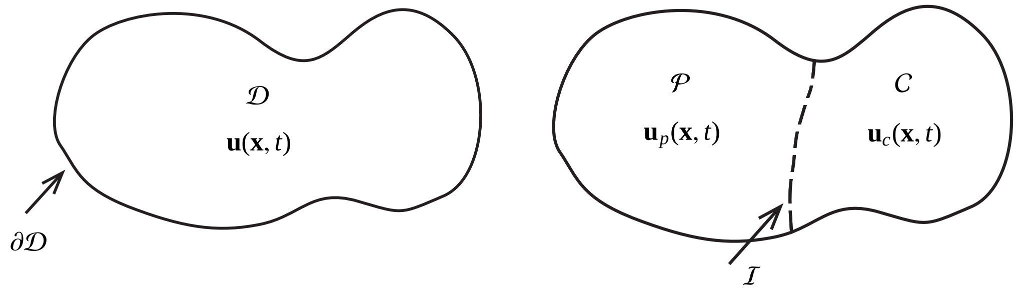

(a)

(b)

Figure 2: (a) A general system with domain $\mathcal{D}$ and state vector $\mathbf{u}(\mathbf{x}, t)$. (b) A general system with imposed separation into two substructures for comparison to the hybrid system. $\mathcal{P} \cup \mathcal{I} \cup C = \mathcal{D}$ and $\partial\mathcal{P} \cap \partial C = \mathcal{I}$.

$$\mathbf{u}(\mathbf{x}, t) \text{ for } \mathbf{x} \in \mathcal{D}. \tag{1}$$

In order to compare the reference system response to the hybrid system response, we can imagine that the reference system is split into two substructures: a "physical" substructure ($\mathcal{P}$-side) and a "computational" substructure (C-side) as shown in Fig. 2b, where $\mathcal{P} \cup \mathcal{I} \cup C = \mathcal{D}$ and $\partial\mathcal{P} \cap \partial C = \mathcal{I}$. The state vector can now be separated into two parts:

$$\mathbf{u}(\mathbf{x}, t) = \begin{cases} \mathbf{u}_p(\mathbf{x}, t) & \text{if } \mathbf{x} \in \mathcal{P} \\ \mathbf{u}_c(\mathbf{x}, t) & \text{if } \mathbf{x} \in C. \end{cases} \tag{2}$$

This defines the true response for a given mechanical system. The precise expression for $\mathbf{u}(\mathbf{x}, t)$ is found by determining the function that satisfies the governing equations of motion on $\mathcal{D}$ and the imposed boundary conditions on $\partial\mathcal{D}$.

2.2. The Hybrid System

The response of the hybrid system should be defined in a similar fashion to make the comparison between the two systems straight forward. Using the same boundary defined in Fig. 2b, the hybrid system is separated into two substructures. In order to differentiate the reference system from the hybrid system a superposed hat (̂) is used to indicate a quantity in the hybrid system. The mechanical response of the hybrid system is represented by the following state vector:

$$\hat{\mathbf{u}}(\mathbf{x}, t) = \begin{cases} \hat{\mathbf{u}}_p(\mathbf{x}, t) & \text{if } \mathbf{x} \in \mathcal{P} \\ \hat{\mathbf{u}}_c(\mathbf{x}, t) & \text{if } \mathbf{x} \in C. \end{cases} \tag{3}$$

In a hybrid system $\hat{\mathbf{u}}_p$ and $\hat{\mathbf{u}}_c$ are determined from the "solution" of the governing equations of motion for $\mathcal{P}$ and C subjected to the boundary conditions on $\partial\mathcal{P}$ and ∂C. The boundary conditions on $\partial\mathcal{D}\cap\partial\mathcal{P}$ and $\partial\mathcal{D}\cap\partial C$ naturally match those of the reference system. However, in the hybrid system one must additionally deal with boundary conditions on the two interface sides $\mathcal{I}_p$ and $\mathcal{I}_c$, where $\mathcal{I}_p = \mathcal{I} \cap \partial\mathcal{P}$ and $\mathcal{I}_c = \mathcal{I} \cap \partial C$. The boundary conditions on $\mathcal{I}_p$ and $\mathcal{I}_c$ are provided by the sensor and actuator system.

The hybrid split leads to more unknowns than equations. To resolve this issue, we need a model of the actuator and sensor system. A relatively general form for such a model can be expressed as [15, 17]:

$$\underline{D}_c[\hat{\mathbf{u}}_c]\Big|_{\mathcal{I}_c} = \underline{D}_p[\hat{\mathbf{u}}_p]\Big|_{\mathcal{I}_p}, \tag{4}$$

where $\underline{D}_c[\bullet]$ and $\underline{D}_p[\bullet]$ are operators that generate the necessary equations at the interface from the state vectors $\hat{\mathbf{u}}_\bullet$. Later in this paper, a simple spring-mass damper system with a PI controller will be used to model the interface,

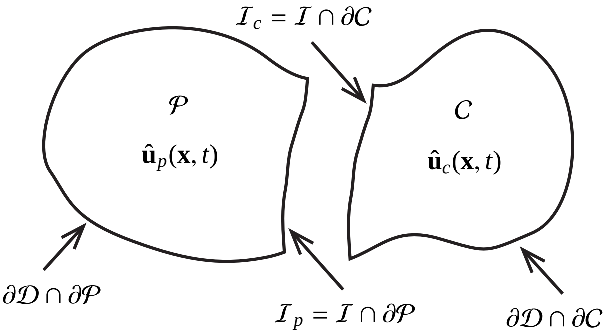

Figure 3: The hybrid system separated into the physical, $\mathcal{P}$, and computational, C, substructures.

and thus allows us to precisely specify the form of $\underline{D}_c[\bullet]$ and $\underline{D}_p[\bullet]$. This model allows one to study the effects of systematic hybrid system splitting errors, specifically boundary mismatch errors. Such errors directly correlate to errors seen in experimental hybrid systems; see e.g. [3, 19].

In an actual hybrid simulation, one only has the physical part $\mathcal{P}$, the sensor and actuator system, and the computational model for part C. In particular one does not have full physical domain $\mathcal{D}$ or the true physical response over $\mathcal{D}$, and this makes it challenging to know if the determined response $\hat{\mathbf{u}}$ is correct to a sufficient degree. To circumvent this issue we will work with an analytical model for the domain $\mathcal{D}$ (and thus we do know the true response over $\mathcal{D}$); further, we do the same for part $\mathcal{P}$ and part C as well as for the sensor and actuator system. This will allow us to faithfully compute the error in the response quantity $\hat{\mathbf{u}}$ of the hybrid system by comparing it to the response quantity $\mathbf{u}$ of the reference system. The error investigated is then strictly the error in the hybrid system associated with the splitting interface. No physical models are involved and the exercise can be fully carried out analytically.

3. Crane System Setup: Equations of Motion

This paper uses a crane structure, specifically a boom crane structure, to test hybrid simulation theoretically. Multiple models already exist for these types of cranes [20, 21, 22], and we use those as the basis for the model used in this paper.

3.1. The Reference System

First we need to setup the model for the crane that is used as a reference for which all subsequent hybrid systems will be compared. The reference system (RS) is that of a station boom crane. For the model in this paper, the crane consists of a supporting beam structure with eight degrees of freedom given by u_1 to u_8. Connected to the crane structure is the crane cabin, which is a rigid body that can rotate about a pivot with a prescribed angel α and a flexing angle δ from the supporting structure. A flexible boom is connected to the cabin, and can pivot with respect to the cabin by some prescribed angle β and a flexing angle γ. Finally, a payload point mass is attached to the end of the boom via an extensible cable defined by a set of spherical polar coordinates, ϕ and θ and radius R. A diagram of the described crane structure can be seen in Fig. 4. The crane can be excited by ground motions in the 1-direction (u_{g1}) and 2-direction (u_{g2}).

Next we need to set up the equations of motion for RS. To do this, we employ Lagrange's prescription for the equations of motion, given by Eq. (5) [23].

$$\frac{d}{dt}\left(\frac{\partial T}{\partial \dot{q}^i}\right) - \frac{\partial T}{\partial q^i} + \frac{\partial U}{\partial q^i} + \frac{\partial D}{\partial \dot{q}^i} = 0, \tag{5}$$

where

$$[q^i] = \begin{bmatrix} R & \phi & \theta & \gamma & u_1 & u_2 & u_3 & u_4 & u_5 & u_6 & u_7 & u_8 \end{bmatrix}. \tag{6}$$

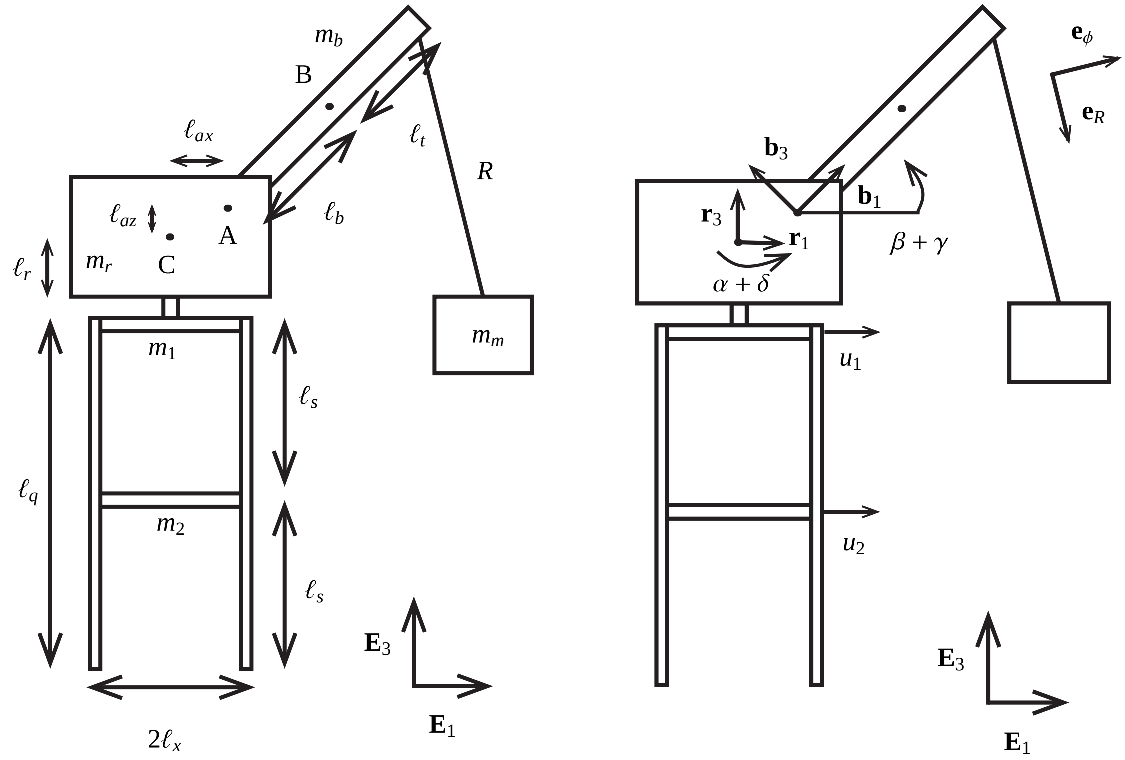

(a) (b)

Figure 4: A diagram of the Reference System (RS).

In this case, T is the kinetic energy, U is the potential energy, and D is the Rayleigh dissipation function(see [24]), which are given by the following:

$$\begin{aligned} T =& \frac{1}{2} m_m \mathbf{v}_m \cdot \mathbf{v}_m + \frac{1}{2} m_b \mathbf{v}_b \cdot \mathbf{v}_b + \frac{1}{2} m_r \mathbf{v}_r \cdot \mathbf{v}_r \\ &+ \frac{1}{2} \omega_b \cdot \mathbf{J}_b \omega_b + \frac{1}{2} \omega_r \cdot \mathbf{J}_r \omega_r + \frac{1}{2} \sum_{j=1}^{4} \dot{\mathbf{u}}_j^t \cdot \mathbf{M}_j \dot{\mathbf{u}}_j^t, \end{aligned} \tag{7}$$

$$\begin{aligned} U =& m_m g \mathbf{x}_m \cdot \mathbf{E}_3 + m_b g \mathbf{x}_b \cdot \mathbf{E}_3 + m_r g \mathbf{x}_r \cdot \mathbf{E}_3 \\ &+ \frac{1}{2} k_m (R - R_0)^2 + \frac{1}{2} k_b \gamma^2 + \frac{1}{2} \sum_{j=1}^{4} \mathbf{u}_j \cdot \mathbf{K}_j \mathbf{u}_j, \end{aligned} \tag{8}$$

$$D = \frac{1}{2} c_m \dot{R}^2 + \frac{1}{2} c_b \dot{\gamma}^2 + \frac{1}{2} \sum_{j=1}^{4} \dot{\mathbf{u}}_j \cdot \mathbf{C}_j \dot{\mathbf{u}}_j, \tag{9}$$

where m_m, c_m, and k_m are the mass, viscous damping constant, and stiffness of the payload and it's cable attachment, m_b, c_b, k_b, and $\mathbf{J}_b$ are the mass, viscous damping constant, stiffness, and rotational inertia matrix of the crane boom, m_r and $\mathbf{J}_r$ are the mass and rotational inertia matrix of the crane cabin, and $\mathbf{M}_j$, $\mathbf{C}_j$, and $\mathbf{K}_j$ are the *jth* mass, damping, and stiffness matrices for the crane supporting structure and are derived following the methods outlined by Chopra [25]. And $\mathbf{u}_j$ are the displacements for the supporting structure. The index j goes from 1 to 4, one for each side of the supporting structure.

First, we define position vectors used to describe the motion of RS:

$$\mathbf{x}_g = u_{g1}\mathbf{E}_1 + u_{g2}\mathbf{E}_2, \tag{10}$$

which is the ground motion.

$$\mathbf{x}_s = 0.5(u_1 + u_5)\mathbf{E}_1 + 0.5(u_3 + u_7)\mathbf{E}_2 + \ell_q\mathbf{E}_3 + \mathbf{x}_g = x_s\mathbf{E}_1 + y_s\mathbf{E}_2 + \ell_q\mathbf{E}_3, \tag{11}$$

which is the position of the base of the crane cabin.

$$\mathbf{x}_r = \ell_r\mathbf{E}_3 + \mathbf{x}_s, \tag{12}$$

which is the center of mass of the crane cabin.

$$\mathbf{x}_a = \ell_{ax}\mathbf{r}_1 + \ell_{az}\mathbf{E}_3 + \mathbf{x}_r, \tag{13}$$

which is the position of the connection point of the boom.

$$\mathbf{x}_b = \ell_b\mathbf{b}_1 + \mathbf{x}_a, \tag{14}$$

which is the center of mass of the boom.

$$\mathbf{x}_t = \ell_t\mathbf{b}_1 + \mathbf{x}_b, \tag{15}$$

which is the position of the end of the boom.

$$\mathbf{x}_m = R\mathbf{e}_R + \mathbf{x}_t, \tag{16}$$

which is the position of the payload.

$$\mathbf{u}_j = [u_{2j-1} \;\; u_{2j}]^T, \tag{17}$$

which are the displacements of the supporting structure. Also, we have

$$\begin{gathered} x_s = 0.5(u_1 + u_5) + u_{g1}, \;\; y_s = 0.5(u_3 + u_7) + u_{g2}, \\ \delta = 0.25\Big(\frac{u_1 - u_5}{l_x} + \frac{u_3 - u_7}{l_y}\Big). \end{gathered} \tag{18}$$

Also, we define the following vectors and rotation tensors:

$$\mathbf{r}_i = \mathbf{R}_1\mathbf{E}_i, \tag{19}$$

where $\mathbf{r}_i$ is the co-rotational basis of the crane cabin.

$$\mathbf{b}_i = \mathbf{R}_2\mathbf{r}_i, \tag{20}$$

where $\mathbf{b}_i$ is the co-rotational basis of the boom.

$$\mathbf{R}_1 = \begin{bmatrix} \cos(\alpha+\delta) & -\sin(\alpha+\delta) & 0 \\ \sin(\alpha+\delta) & \cos(\alpha+\delta) & 0 \\ 0 & 0 & 1 \end{bmatrix}_{\mathbf{E}_i\otimes\mathbf{E}_j} \tag{21}$$

is the rotation tensor from the Cartesian basis to the $\mathbf{r}_i$ basis.

$$\mathbf{R}_2 = \begin{bmatrix} \cos(\beta+\gamma) & 0 & -\sin(\beta+\gamma) \\ 0 & 1 & 0 \\ \sin(\beta+\gamma) & 0 & \cos(\beta+\gamma) \end{bmatrix}_{\mathbf{r}_i\otimes\mathbf{r}_j} \tag{22}$$

is the rotation tensor from the $\mathbf{r}_i$ basis to the $\mathbf{b}_i$ basis.

$$\mathbf{e}_R = \cos(\theta)\sin(\phi)\mathbf{E}_1 + \cos(\phi)\mathbf{E}_2 - \sin(\theta)\sin(\phi)\mathbf{E}_3, \tag{23}$$

$$\mathbf{e}_\phi = \cos(\theta)\cos(\phi)\mathbf{E}_1 - \sin(\phi)\mathbf{E}_2 - \sin(\theta)\cos(\phi)\mathbf{E}_3, \tag{24}$$

and

$$\mathbf{e}_\theta = -\sin(\theta)\mathbf{E}_1 - \cos(\theta)\mathbf{E}_3, \tag{25}$$

define the spherical basis vectors used to define the position of the payload. Next we define the velocity vectors for the system:

$$\mathbf{v}_g = \dot{u}_{g1}\mathbf{E}_1 + \dot{u}_{g1}\mathbf{E}_2, \tag{26}$$

$$\mathbf{v}_s = 0.5(\dot{u}_1 + \dot{u}_5)\mathbf{E}_1 + 0.5(\dot{u}_3 + \dot{u}_7)\mathbf{E}_2 + \mathbf{v}_g = \dot{x}_s\mathbf{E}_1 + \dot{y}_s\mathbf{E}_2, \tag{27}$$

$$\mathbf{v}_r = \mathbf{v}_s, \tag{28}$$

$$\mathbf{v}_a = \ell_{ax}(\dot{\alpha} + \dot{\delta})\mathbf{r}_2 + \mathbf{v}_r, \tag{29}$$

$$\mathbf{v}_b = \ell_b(\dot{\beta} + \dot{\gamma})\mathbf{b}_3 + \ell_b(\dot{\alpha} + \dot{\delta})\cos(\beta + \gamma)\mathbf{r}_2 + \mathbf{v}_a, \tag{30}$$

$$\mathbf{v}_t = \ell_t(\dot{\beta} + \dot{\gamma})\mathbf{b}_3 + \ell_t(\dot{\alpha} + \dot{\delta})\cos(\beta + \gamma)\mathbf{r}_2 + \mathbf{v}_b, \tag{31}$$

$$\mathbf{v}_m = \dot{R}\mathbf{e}_R + R\dot{\theta}\mathbf{e}_\phi + R\sin(\phi)\dot{\theta}\mathbf{e}_\theta + \mathbf{v}_t, \tag{32}$$

$$\dot{\mathbf{u}}^t_j = [\dot{u}_{2j-1} \;\; \dot{u}_{2j}]^T - \begin{cases} [\dot{u}_{g1} \;\; \dot{u}_{g1}]^T \text{ if } j \text{ is odd} \\ [\dot{u}_{g2} \;\; \dot{u}_{g2}]^T \text{ if } j \text{ is even,} \end{cases} \tag{33}$$

where Eqs. (26)-(33) are the velocities of the corresponding positions defined in Eqs. (10)-(17). Also, the angular velocities of the crane cabin and boom are

$$\boldsymbol{\omega}_r = (\dot{\alpha} + \dot{\delta})\mathbf{E}_3, \tag{34}$$

and

$$\boldsymbol{\omega}_b = -(\dot{\beta} + \dot{\gamma})\mathbf{r}_2 + \boldsymbol{\omega}_r, \tag{35}$$

respectively.

The previous equations give all of the necessary information to expand Eq. (5) to give the 12 equations of motion that can then be solved using a numerical integrator.

3.2. The First Hybrid System

Next, we set up the first hybrid system (HS1). In this case, the hybrid split is applied at the connection between the supporting structure and cabin, as can be seen in Fig. 5. In this case, the supporting structure is considered the computational side, or $\mathcal{C}$-side, and everything else is considered the physical side, or $\mathcal{P}$-side. By introducing this hybrid split, we introduce three new degrees of freedom: x_{sp}, y_{sp}, and δ_p which are the $\mathbf{E}_1$ position, $\mathbf{E}_2$ position, and rotation angle of the base of the crane cabin from the physical side.

Again, the equations of motion are determined by Lagrange's prescription, given by

$$\begin{aligned} \frac{d}{dt}\left(\frac{\partial \hat{T}_1}{\partial \dot{\hat{q}}^i_1}\right) - \frac{\partial \hat{T}_1}{\partial \hat{q}^i_1} + \frac{\partial \hat{U}_1}{\partial \hat{q}^i_1} + \frac{\partial \hat{D}_1}{\partial \dot{\hat{q}}^i_1} =& \mathbf{F}_{1p} \cdot \frac{\partial \mathbf{v}_{sp}}{\partial \dot{\hat{q}}^i_1} + \mathbf{F}_{1c} \cdot \frac{\partial \mathbf{v}_{sc}}{\partial \dot{\hat{q}}^i_1} \\ &+ \mathbf{M}_{1p} \cdot \frac{\partial \boldsymbol{\omega}_{rp}}{\partial \dot{\hat{q}}^i_1} + \mathbf{M}_{1c} \cdot \frac{\partial \boldsymbol{\omega}_{rc}}{\partial \dot{\hat{q}}^i_1}, \end{aligned} \tag{36}$$

where

$$[\hat{q}^i_1] = \begin{bmatrix} R & \phi & \theta & \gamma & x_{sp} & y_{sp} & \delta_p & u_1 & u_2 & u_3 & u_4 & u_5 & u_6 & u_7 & u_8 \end{bmatrix}. \tag{37}$$

Note, that a superposed hat ($\hat{\ }$) is used to denote a quantity for a hybrid system. Again, $\hat{T}_1$ is the kinetic energy, $\hat{U}_1$ is the potential energy, and $\hat{D}_1$ is the Rayleigh dissipation function, defined as:

$$\begin{aligned} \hat{T}_1 =& \frac{1}{2}m_m\mathbf{v}_m \cdot \mathbf{v}_m + \frac{1}{2}m_b\mathbf{v}_b \cdot \mathbf{v}_b + \frac{1}{2}m_r\mathbf{v}_r \cdot \mathbf{v}_r \\ &+ \frac{1}{2}\boldsymbol{\omega}_b \cdot \mathbf{J}_b\boldsymbol{\omega}_b + \frac{1}{2}\boldsymbol{\omega}_r \cdot \mathbf{J}_r\boldsymbol{\omega}_r + \frac{1}{2}\sum_{j=1}^{4}\dot{\mathbf{u}}^t_j \cdot \mathbf{M}_j\dot{\mathbf{u}}^t_j, \end{aligned} \tag{38}$$

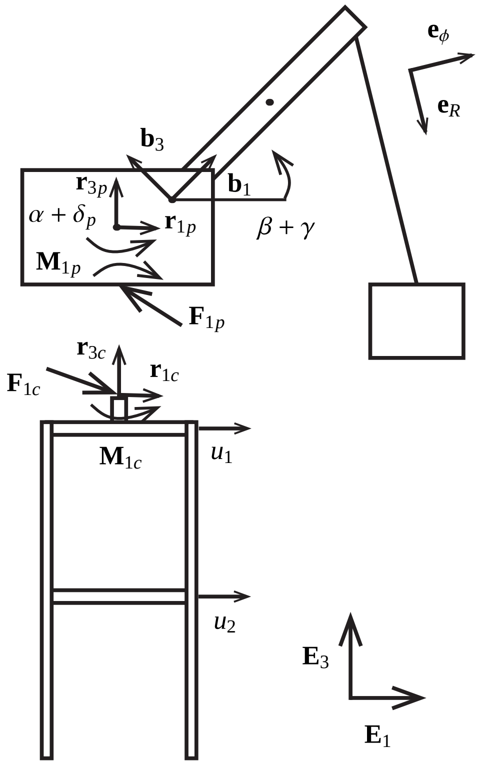

Figure 5: A diagram of the First Hybrid System (HS1).

$$\begin{aligned} \hat{U}_1 = & m_m g \mathbf{x}_m \cdot \mathbf{E}_3 + m_b g \mathbf{x}_b \cdot \mathbf{E}_3 + m_r g \mathbf{x}_r \cdot \mathbf{E}_3 \\ & + \frac{1}{2} k_m (R - R_0)^2 + \frac{1}{2} k_b \gamma^2 + \frac{1}{2} \sum_{j=1}^{4} \mathbf{u}_j \cdot \mathbf{K}_j \mathbf{u}_j, \end{aligned} \tag{39}$$

$$\hat{D}_1 = \frac{1}{2} c_m \dot{R}^2 + \frac{1}{2} c_b \dot{\gamma}^2 + \frac{1}{2} \sum_{j=1}^{4} \dot{\mathbf{u}}_j \cdot \mathbf{C}_j \dot{\mathbf{u}}_j. \tag{40}$$

Note that all of the physical quantities, such as masses, stiffness, lengths, etc. are the same as those for RS. For HS1 we have the additional terms of $\mathbf{F}_{1p}$, $\mathbf{F}_{1c}$, $\mathbf{M}_{1p}$, and $\mathbf{M}_{1c}$. In this case, $\mathbf{F}_{1p}$ and $\mathbf{M}_{1p}$ represent the force and moment read by sensors on the physical substructure, and $\mathbf{F}_{1c}$ and $\mathbf{M}_{1c}$ are the force and moment used as inputs to the computational model. We now define the position vectors for HS1:

$$\mathbf{x}_g = u_{g1} \mathbf{E}_1 + u_{g2} \mathbf{E}_2, \tag{41}$$

$$\mathbf{x}_{sc} = 0.5(u_1 + u_5)\mathbf{E}_1 + 0.5(u_3 + u_7)\mathbf{E}_2 + \ell_q \mathbf{E}_3 + \mathbf{x}_g = x_{sc} \mathbf{E}_1 + y_{sc} \mathbf{E}_2 + \ell_q \mathbf{E}_3, \tag{42}$$

$$\mathbf{x}_{sp} = x_{sp} \mathbf{E}_1 + y_{sp} \mathbf{E}_2 + \ell_q \mathbf{E}_3, \tag{43}$$

$$\mathbf{x}_r = \ell_r \mathbf{E}_3 + \mathbf{x}_{sp}, \tag{44}$$

$$\mathbf{x}_a = \ell_{ax} \mathbf{r}_{1p} + \ell_{az} \mathbf{E}_3 + \mathbf{x}_r, \tag{45}$$

$$\mathbf{x}_b = \ell_b \mathbf{b}_1 + \mathbf{x}_a, \tag{46}$$

$$\mathbf{x}_t = \ell_t \mathbf{b}_1 + \mathbf{x}_b, \tag{47}$$

$$\mathbf{x}_m = R\mathbf{e}_R + \mathbf{x}_t, \tag{48}$$

$$\mathbf{u}_j = [u_{2j-1} \;\; u_{2j}]^T, \tag{49}$$

where Eqs. (41)-(49) have the same physical meaning as their corresponding Eqs. (10)-(17), except that $\mathbf{x}_{sc}$ defines the position of the base of the crane cabin from the computational side and $\mathbf{x}_{sp}$ defines the position of the base of the crane cabin from the physical side. Where the following quantities are defined as:

$$\begin{aligned} x_{sc} =& 0.5(u_1 + u_5) + u_{g1}, \;\; y_{sc} = 0.5(u_3 + u_7) + u_{g2}, \\ \delta_c =& 0.25\Big(\frac{u_1 - u_5}{l_x} + \frac{u_3 - u_7}{l_y}\Big). \end{aligned} \tag{50}$$

We also define the following vectors and rotation tensors:

$$\mathbf{r}_{ip} = \mathbf{R}_{1p}\mathbf{E}_i, \tag{51}$$

where $\mathbf{r}_{ip}$ is the co-rotational basis for the crane cabin, which is on the physical side.

$$\mathbf{b}_i = \mathbf{R}_2\mathbf{r}_{ip}, \tag{52}$$

where $\mathbf{b}_i$ is the co-rotational basis for the boom.

$$\mathbf{R}_{1p} = \begin{bmatrix} \cos(\alpha + \delta_p) & -\sin(\alpha + \delta_p) & 0 \\ \sin(\alpha + \delta_p) & \cos(\alpha + \delta_p) & 0 \\ 0 & 0 & 1 \end{bmatrix}_{\mathbf{E}_i \otimes \mathbf{E}_j} \tag{53}$$

is the rotation tensor from the Cartesian basis to the $\mathbf{r}_{ip}$ basis.

$$\mathbf{R}_2 = \begin{bmatrix} \cos(\beta + \gamma) & 0 & -\sin(\beta + \gamma) \\ 0 & 1 & 0 \\ \sin(\beta + \gamma) & 0 & \cos(\beta + \gamma) \end{bmatrix}_{\mathbf{r}_{ip} \otimes \mathbf{r}_{jp}} \tag{54}$$

is the rotation tensor from the $\mathbf{r}_{ip}$ basis to the $\mathbf{b}_i$ basis.

$$\mathbf{e}_R = \cos(\theta)\sin(\phi)\mathbf{E}_1 + \cos(\phi)\mathbf{E}_2 - \sin(\theta)\sin(\phi)\mathbf{E}_3, \tag{55}$$

$$\mathbf{e}_\phi = \cos(\theta)\cos(\phi)\mathbf{E}_1 - \sin(\phi)\mathbf{E}_2 - \sin(\theta)\cos(\phi)\mathbf{E}_3, \tag{56}$$

and

$$\mathbf{e}_\theta = -\sin(\theta)\mathbf{E}_1 - \cos(\theta)\mathbf{E}_3, \tag{57}$$

define the spherical basis vectors to define the position of the payload. Next we define the velocity vectors for HS1:

$$\mathbf{v}_g = \dot{u}_{g1}\mathbf{E}_1 + \dot{u}_{g2}\mathbf{E}_2, \tag{58}$$

$$\mathbf{v}_{sc} = 0.5(\dot{u}_1 + \dot{u}_5)\mathbf{E}_1 + 0.5(\dot{u}_3 + \dot{u}_7)\mathbf{E}_2 + \mathbf{v}_g = \dot{x}_{sc}\mathbf{E}_1 + \dot{y}_{sc}\mathbf{E}_2, \tag{59}$$

$$\mathbf{v}_{sp} = \dot{x}_{sp}\mathbf{E}_1 + \dot{y}_{sp}\mathbf{E}_2, \tag{60}$$

$$\mathbf{v}_r = \mathbf{v}_{sp}, \tag{61}$$

$$\mathbf{v}_a = \ell_{ax}(\dot{\alpha} + \dot{\delta}_p)\mathbf{r}_{2p} + \mathbf{v}_r, \tag{62}$$

$$\mathbf{v}_b = \ell_b(\dot{\beta} + \dot{\gamma})\mathbf{b}_3 + \ell_b(\dot{\alpha} + \dot{\delta}_p)\cos(\beta + \gamma)\mathbf{r}_{2p} + \mathbf{v}_a, \tag{63}$$

$$\mathbf{v}_t = \ell_t(\dot{\beta} + \dot{\gamma})\mathbf{b}_3 + \ell_t(\dot{\alpha} + \dot{\delta}_p)\cos(\beta + \gamma)\mathbf{r}_{2p} + \mathbf{v}_b, \tag{64}$$

$$\mathbf{v}_m = \dot{R}\mathbf{e}_R + R\dot{\theta}\mathbf{e}_\phi + R\sin(\phi)\dot{\theta}\mathbf{e}_\theta + \mathbf{v}_t, \tag{65}$$

$$\dot{\mathbf{u}}^t_j = [\dot{u}_{2j-1} \;\; \dot{u}_{2j}]^T - \begin{cases} [\dot{u}_{g1} \;\; \dot{u}_{g1}]^T \text{ if } j \text{ is odd} \\ [\dot{u}_{g2} \;\; \dot{u}_{g2}]^T \text{ if } j \text{ is even,} \end{cases} \tag{66}$$

where Eqs. (58)-(66) are the velocity vectors of the corresponding position vectors from Eqs. (41)-(49). We also define the following angular velocity vectors:

$$\boldsymbol{\omega}_{rc} = (\dot{\alpha} + \dot{\delta}_c)\mathbf{E}_3, \tag{67}$$

which is the rotational velocity of the crane cabin from the computational side.

$$\boldsymbol{\omega}_{rp} = (\dot{\alpha} + \dot{\delta}_p)\mathbf{E}_3, \tag{68}$$

which is the rotational velocity of the crane cabin from the physical side.

$$\boldsymbol{\omega}_b = -(\dot{\beta} + \dot{\gamma})\mathbf{r}_{2p} + \boldsymbol{\omega}_{rp}, \tag{69}$$

which is the rotational velocity of the boom.

In the ideal setting (i.e. no sensor error), we have

$$\mathbf{F}_{1c} \cdot \mathbf{E}_1 = -\mathbf{F}_{1p} \cdot \mathbf{E}_1, \;\; \mathbf{F}_{1c} \cdot \mathbf{E}_2 = -\mathbf{F}_{1p} \cdot \mathbf{E}_2, \;\; \mathbf{M}_{1c} \cdot \mathbf{E}_3 = -\mathbf{M}_{1p} \cdot \mathbf{E}_3. \tag{70}$$

However, at this point, we do not have enough equations to fully determine the motion of HS1. In order to get the remaining equations, we need a model for the error at the hybrid split. For this paper, the error is modeled as a spring-mass-damper system controlled by a PI controller [26]. For the error model chosen, we follow the definition of Drazin [15] for internal boundary conditions, or

$$\underline{D}_c[\hat{\mathbf{u}}_{c1}]\Big|_{\mathcal{I}_{c1}} = \underline{D}_p[\hat{\mathbf{u}}_{p1}]\Big|_{\mathcal{I}_{p1}}. \tag{71}$$

In this case $\hat{\mathbf{u}}_{c1}$ and $\hat{\mathbf{u}}_{p1}$ are given by

$$\hat{\mathbf{u}}_{c1} = \begin{bmatrix} x_{sc} & y_{sc} & \delta_c \end{bmatrix}^T, \qquad \hat{\mathbf{u}}_{p1} = \begin{bmatrix} x_{sp} & y_{sp} & \delta_p \end{bmatrix}^T, \tag{72}$$

where the operators $\underline{D}_c[\hat{\mathbf{u}}_{c1}]$ and $\underline{D}_p[\hat{\mathbf{u}}_{p1}]$ have the following definitions:

$$\underline{D}_c[\hat{\mathbf{u}}_{c1}] = \Big(k_a k_i + (k_a k_p + c_a k_i)\frac{d}{dt} + c_a k_p \frac{d^2}{dt^2}\Big)\hat{\mathbf{u}}_{c1}, \tag{73}$$

and

$$\underline{D}_p[\hat{\mathbf{u}}_{p1}] = \Big(k_a k_i + (k_a(1 + k_p) + c_a k_i)\frac{d}{dt} + (c_a(1 + k_p))\frac{d^2}{dt^2} + m_a \frac{d^3}{dt^3}\Big)\hat{\mathbf{u}}_{p1}, \tag{74}$$

where the parameters m_a, c_a, and k_a are the mass, damping constant, and stiffness of the spring-mass-damper system used to model the actuator. The parameters k_p and k_i are the proportional and integral gains of the PI controller. Now we have an equal number of unknowns as we have equations, which allows to solve the equations of motion for HS1 with the use of a numerical integrator.

3.3. The Second Hybrid System

The second hybrid system (HS2) has the hybrid split applied to the boom-cabin joint. A diagram of HS2 can be seen in Fig. 6. In this case, the supporting structure and cabin are considered the physical substructure, $\mathcal{P}$-side, and everything else is considered the computational model, $\mathcal{C}$-side. By introducing this hybrid split, we introduce three new degrees of freedom: x_{ac}, y_{ac}, and δ_c, which are the $\mathbf{E}_1$ position, the $\mathbf{E}_2$ position, and rotation angle of the connection point between the crane cabin and boom from the computational side. Lagrange's equations for HS2 are

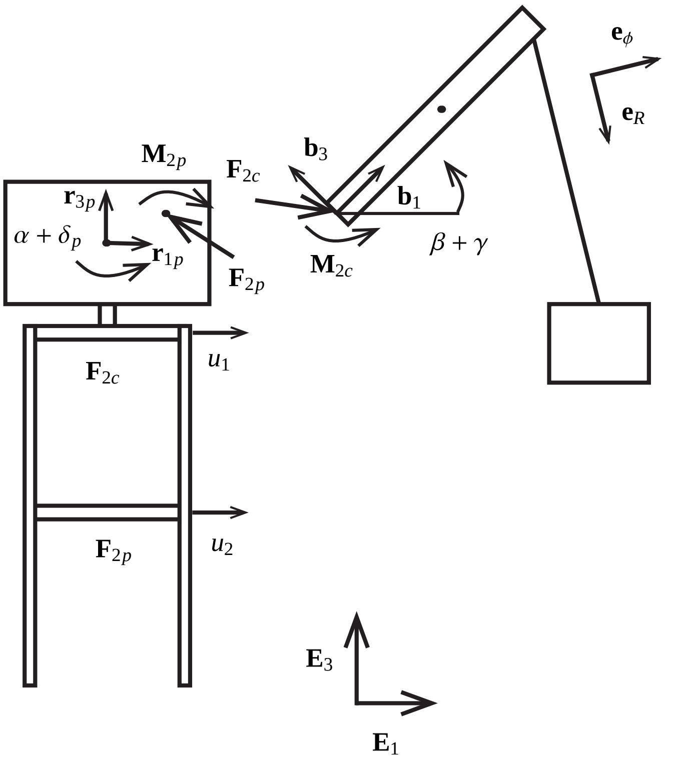

Figure 6: A diagram of the Second Hybrid System (HS2).

given by

$$\frac{d}{dt}\left(\frac{\partial \hat{T}_2}{\partial \dot{\hat{q}}_2^i}\right) - \frac{\partial \hat{T}_2}{\partial \hat{q}_2^i} + \frac{\partial \hat{U}_2}{\partial \hat{q}_2^i} + \frac{\partial \hat{D}_2}{\partial \dot{\hat{q}}_2^i} = \mathbf{F}_{2p} \cdot \frac{\partial \mathbf{v}_{ap}}{\partial \dot{\hat{q}}_2^i} + \mathbf{F}_{2c} \cdot \frac{\partial \mathbf{v}_{ac}}{\partial \dot{\hat{q}}_2^i} + \mathbf{M}_{2p} \cdot \frac{\partial \boldsymbol{\omega}_{rp}}{\partial \dot{\hat{q}}_2^i} + \mathbf{M}_{2c} \cdot \frac{\partial \boldsymbol{\omega}_{rc}}{\partial \dot{\hat{q}}_2^i}, \tag{75}$$

where

$$\left[\hat{q}_2^i\right] = \begin{bmatrix} R & \phi & \theta & \gamma & x_{ac} & y_{ac} & \delta_c & u_1 & u_2 & u_3 & u_4 & u_5 & u_6 & u_7 & u_8 \end{bmatrix}. \tag{76}$$

The kinetic energy, $\hat{T}_2$, the potential energy, $\hat{U}_2$, and the Rayleigh dissipation function, $\hat{D}_2$, are defined as follows:

$$\hat{T}_2 = \frac{1}{2} m_m \mathbf{v}_m \cdot \mathbf{v}_m + \frac{1}{2} m_b \mathbf{v}_b \cdot \mathbf{v}_b + \frac{1}{2} m_r \mathbf{v}_r \cdot \mathbf{v}_r + \frac{1}{2} \boldsymbol{\omega}_b \cdot \mathbf{J}_b \boldsymbol{\omega}_b + \frac{1}{2} \boldsymbol{\omega}_r \cdot \mathbf{J}_r \boldsymbol{\omega}_r + \frac{1}{2} \sum_{j=1}^{4} \dot{\mathbf{u}}_j^t \cdot \mathbf{M}_j \dot{\mathbf{u}}_j^t, \tag{77}$$

$$\hat{U}_2 = m_m g \mathbf{x}_m \cdot \mathbf{E}_3 + m_b g \mathbf{x}_b \cdot \mathbf{E}_3 + m_r g \mathbf{x}_r \cdot \mathbf{E}_3 + \frac{1}{2} k_m (R - R_0)^2 + \frac{1}{2} k_b \gamma^2 + \frac{1}{2} \sum_{j=1}^{4} \mathbf{u}_j \cdot \mathbf{K}_j \mathbf{u}_j, \tag{78}$$

$$\hat{D}_2 = \frac{1}{2} c_m \dot{R}^2 + \frac{1}{2} c_b \dot{\gamma}^2 + \frac{1}{2} \sum_{j=1}^{4} \dot{\mathbf{u}}_j \cdot \mathbf{C}_j \dot{\mathbf{u}}_j. \tag{79}$$

For HS2, we introduce $\mathbf{F}_{2p}$, $\mathbf{F}_{2c}$, $\mathbf{M}_{2p}$, and $\mathbf{M}_{2c}$. In this case, $\mathbf{F}_{2p}$ and $\mathbf{M}_{2p}$ represent the force and moment read by sensors on the physical substructure, and $\mathbf{F}_{2c}$ and $\mathbf{M}_{2c}$ are the force and moment used as inputs to the computational model. We now define the position vectors:

$$\mathbf{x}_g = u_{g1}\mathbf{E}_1 + u_{g2}\mathbf{E}_2, \tag{80}$$

$$\mathbf{x}_s = 0.5(u_1 + u_5)\mathbf{E}_1 + 0.5(u_3 + u_7)\mathbf{E}_2 + \ell_q\mathbf{E}_3 + \mathbf{x}_g = x_{sp}\mathbf{E}_1 + y_{sp}\mathbf{E}_2 + \ell_q\mathbf{E}_3, \tag{81}$$

$$\mathbf{x}_r = \ell_r\mathbf{E}_3 + \mathbf{x}_s, \tag{82}$$

$$\mathbf{x}_{ap} = \ell_{ax}\mathbf{r}_{1p} + \ell_{az}\mathbf{E}_3 + \mathbf{x}_r = x_{ap}\mathbf{E}_1 + y_{ap}\mathbf{E}_2 + (\ell_q + \ell_c + \ell_{az})\mathbf{E}_3, \tag{83}$$

$$\mathbf{x}_{ac} = x_{ac}\mathbf{E}_1 + y_{ac}\mathbf{E}_2 + (\ell_q + \ell_c + \ell_{az})\mathbf{E}_3, \tag{84}$$

$$\mathbf{x}_b = \ell_b\mathbf{b}_1 + \mathbf{x}_{ac}, \tag{85}$$

$$\mathbf{x}_t = \ell_t\mathbf{b}_1 + \mathbf{x}_b, \tag{86}$$

$$\mathbf{x}_m = R\mathbf{e}_R + \mathbf{x}_t, \tag{87}$$

$$\mathbf{u}_j = [u_{2j-1}\ \ u_{2j}]^T, \tag{88}$$

where Eqs. (80)-(88) have the same physical meaning as the corresponding Eqs. (10)-(17), except that $\mathbf{x}_{ac}$ is the position of the connection point between the crane cabin and the boom from the computational side and $\mathbf{x}_{ap}$ is the position of the connection point between the crane cabin and the boom from the physical side. Where the followings quantities are defined as:

$$\begin{aligned} x_{sp} =& 0.5(u_1 + u_5) + u_{g1},\ y_{sp} = 0.5(u_3 + u_7) + u_{g2}, \\ \delta_p =& 0.25\Big(\frac{u_1 - u_5}{l_x} + \frac{u_3 - u_7}{l_y}\Big), \end{aligned} \tag{89}$$

and

$$x_{ap} = x_{sp} + l_{ax}\cos(\alpha + \delta_p),\ y_{ap} = y_{sp} + l_{ax}\sin(\alpha + \delta_p). \tag{90}$$

We also need the following vectors and rotation tensors:

$$\mathbf{r}_{ip} = \mathbf{R}_{1p}\mathbf{E}_i, \tag{91}$$

where $\mathbf{r}_{ip}$ is the co-rotational basis of the crane cabin from the physical side.

$$\mathbf{r}_{ic} = \mathbf{R}_{1c}\mathbf{E}_i, \tag{92}$$

where $\mathbf{r}_{ic}$ is the co-rotational basis of the crane cabin from the computational side.

$$\mathbf{b}_i = \mathbf{R}_2\mathbf{r}_{ic}, \tag{93}$$

where $\mathbf{b}_i$ is the co-rotational basis of the boom.

$$\mathbf{R}_{1p} = \begin{bmatrix} \cos(\alpha + \delta_p) & -\sin(\alpha + \delta_p) & 0 \\ \sin(\alpha + \delta_p) & \cos(\alpha + \delta_p) & 0 \\ 0 & 0 & 1 \end{bmatrix}_{\mathbf{E}_i \otimes \mathbf{E}_j} \tag{94}$$

is the rotation tensor from the Cartesian basis to the $\mathbf{r}_{ip}$ basis.

$$\mathbf{R}_{1c} = \begin{bmatrix} \cos(\alpha + \delta_c) & -\sin(\alpha + \delta_c) & 0 \\ \sin(\alpha + \delta_c) & \cos(\alpha + \delta_c) & 0 \\ 0 & 0 & 1 \end{bmatrix}_{\mathbf{E}_i \otimes \mathbf{E}_j} \tag{95}$$

is the rotation tensor from the Cartesian basis to the $\mathbf{r}_{ic}$ basis.

$$\mathbf{R}_2 = \begin{bmatrix} \cos(\beta+\gamma) & 0 & -\sin(\beta+\gamma) \\ 0 & 1 & 0 \\ \sin(\beta+\gamma) & 0 & \cos(\beta+\gamma) \end{bmatrix}_{\mathbf{r}_{ic}\otimes\mathbf{r}_{jc}} \tag{96}$$

is the rotation tensor from the $\mathbf{r}_{ic}$ basis to the $\mathbf{b}_i$ basis.

$$\mathbf{e}_R = \cos(\theta)\sin(\phi)\mathbf{E}_1 + \cos(\phi)\mathbf{E}_2 - \sin(\theta)\sin(\phi)\mathbf{E}_3, \tag{97}$$

$$\mathbf{e}_\phi = \cos(\theta)\cos(\phi)\mathbf{E}_1 - \sin(\phi)\mathbf{E}_2 - \sin(\theta)\cos(\phi)\mathbf{E}_3, \tag{98}$$

and

$$\mathbf{e}_\theta = -\sin(\theta)\mathbf{E}_1 - \cos(\theta)\mathbf{E}_3, \tag{99}$$

define the spherical basis vectors to define the position of the payload. And the required velocity vectors:

$$\mathbf{v}_g = \dot{u}_{g1}\mathbf{E}_1 + \dot{u}_{g2}\mathbf{E}_2, \tag{100}$$

$$\mathbf{v}_{sp} = 0.5(\dot{u}_1 + \dot{u}_5)\mathbf{E}_1 + 0.5(\dot{u}_3 + \dot{u}_7)\mathbf{E}_2 + \mathbf{v}_g = \dot{x}_{sp}\mathbf{E}_1 + \dot{y}_{sp}\mathbf{E}_2, \tag{101}$$

$$\mathbf{v}_r = \mathbf{v}_{sp}, \tag{102}$$

$$\mathbf{v}_{ap} = \ell_{ax}(\dot{\alpha} + \dot{\delta}_p)\mathbf{r}_{2p} + \mathbf{v}_r, \tag{103}$$

$$\mathbf{v}_{ac} = \dot{x}_{ac}\mathbf{E}_1 + \dot{y}_{ac}\mathbf{E}_2, \tag{104}$$

$$\mathbf{v}_b = \ell_b(\dot{\beta} + \dot{\gamma})\mathbf{b}_3 + \ell_b(\dot{\alpha} + \dot{\delta}_c)\cos(\beta+\gamma)\mathbf{r}_{2c} + \mathbf{v}_{ac}, \tag{105}$$

$$\mathbf{v}_t = \ell_t(\dot{\beta} + \dot{\gamma})\mathbf{b}_3 + \ell_t(\dot{\alpha} + \dot{\delta}_c)\cos(\beta+\gamma)\mathbf{r}_{2c} + \mathbf{v}_b, \tag{106}$$

$$\mathbf{v}_m = \dot{R}\mathbf{e}_R + R\dot{\theta}\mathbf{e}_\phi + R\sin(\phi)\dot{\theta}\mathbf{e}_\theta + \mathbf{v}_t, \tag{107}$$

$$\dot{\mathbf{u}}^t_j = [\dot{u}_{2j-1}\ \ \dot{u}_{2j}]^T - \begin{cases} [\dot{u}_{g1}\ \ \dot{u}_{g1}]^T & \text{if } j \text{ is odd} \\ [\dot{u}_{g2}\ \ \dot{u}_{g2}]^T & \text{if } j \text{ is even,} \end{cases} \tag{108}$$

where Eqs. (100)-(108) are the velocities of the corresponding positions from Eqs. (80)-(88). Also, we have the following angular velocity vectors:

$$\boldsymbol{\omega}_{rc} = (\dot{\alpha} + \dot{\delta}_c)\mathbf{E}_3, \tag{109}$$

which is the angular velocity of the crane cabin from the computational side.

$$\boldsymbol{\omega}_{rp} = (\dot{\alpha} + \dot{\delta}_p)\mathbf{E}_3, \tag{110}$$

which is the angular velocity of the crane cabin from the physical side.

$$\boldsymbol{\omega}_b = -(\dot{\beta} + \dot{\gamma})\mathbf{r}_{2c} + \boldsymbol{\omega}_{rc}, \tag{111}$$

which is the angular velocity of the boom.

In the ideal setting, we have

$$\mathbf{F}_{2c}\cdot\mathbf{E}_1 = -\mathbf{F}_{2p}\cdot\mathbf{E}_1,\ \mathbf{F}_{2c}\cdot\mathbf{E}_2 = -\mathbf{F}_{2p}\cdot\mathbf{E}_2,\ \mathbf{M}_{2c}\cdot\mathbf{E}_3 = -\mathbf{M}_{2p}\cdot\mathbf{E}_3. \tag{112}$$

Again, at this point, there are not enough equations to match the number of unknowns. To get the remaining equations, we use the model for the error at the split. Similar to HS1, the error is modeled as a spring-mass-damper system controlled by a PI controller:

$$\underline{D}_c[\hat{\mathbf{u}}_{c2}]\Big|_{\mathcal{I}_{c2}} = \underline{D}_p[\hat{\mathbf{u}}_{p2}]\Big|_{\mathcal{I}_{p2}}. \tag{113}$$

In this case $\hat{\mathbf{u}}_{c2}$ and $\hat{\mathbf{u}}_{p2}$ are given by

$$\hat{\mathbf{u}}_{c2} = \begin{bmatrix} x_{ac} & y_{ac} & \delta_c \end{bmatrix}^T, \qquad \hat{\mathbf{u}}_{p2} = \begin{bmatrix} x_{ap} & y_{ap} & \delta_p \end{bmatrix}^T, \tag{114}$$

where the operators $\underline{D}_c[\hat{\mathbf{u}}_{c2}]$ and $\underline{D}_p[\hat{\mathbf{u}}_{p2}]$ have the following definitions:

$$\underline{D}_c[\hat{\mathbf{u}}_{c2}] = \Big(k_a k_i + (k_a k_p + c_a k_i)\frac{d}{dt} + c_a k_p \frac{d^2}{dt^2}\Big)\hat{\mathbf{u}}_{c2}, \tag{115}$$

and

$$\underline{D}_p[\hat{\mathbf{u}}_{p2}] = \Big(k_a k_i + (k_a(1 + k_p) + c_a k_i)\frac{d}{dt} + (c_a(1 + k_p))\frac{d^2}{dt^2} + m_a \frac{d^3}{dt^3}\Big)\hat{\mathbf{u}}_{p2}, \tag{116}$$

where the parameters are the same as those for HS1. We now have the required number of equations to solve for the motion of HS2.

3.4. The Third Hybrid System

For the third hybrid system (HS3), we have two hybrid splits. The first split is at the connection between the supporting structure and the cabin. The second split is at the connection between the cabin and the boom. In this case the cabin is considered the physical substructure, $\mathcal{P}$-side, and everything else is considered the computational model, C-side. Introducing these hybrid splits introduces six new degrees of freedom: x_{sp}, y_{sp}, δ_p, x_{ac}, y_{ac}, and δ_{c2}. Where x_{sp}, y_{sp}, and $\delta_p$are the $\mathbf{E}_1$ position, $\mathbf{E}_2$ position, and rotation angle of the base of the crane cabin from the physical side and x_{ac}, y_{ac}, and δ_{c2} are the $\mathbf{E}_1$ position, the $\mathbf{E}_2$ position, and rotation angle of the connection point between the crane cabin and boom from the computational side. A figure of HS3 is shown in Fig. 7.

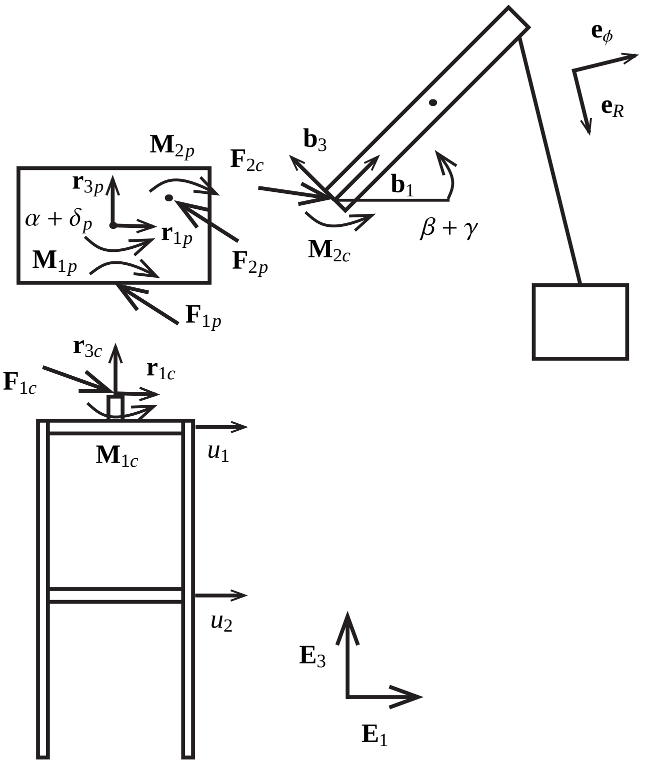

Figure 7: A diagram of the Third Hybrid System (HS3).

Lagrange's equation are given by the following:

$$\begin{aligned}\frac{d}{dt}\left(\frac{\partial \hat{T}_3}{\partial \dot{\hat{q}}_3^i}\right) - \frac{\partial \hat{T}_3}{\partial \hat{q}_3^i} + \frac{\partial \hat{U}_3}{\partial \hat{q}_3^i} + \frac{\partial \hat{D}_3}{\partial \dot{\hat{q}}_3^i} =& \mathbf{F}_{1p} \cdot \frac{\partial \mathbf{v}_{sp}}{\partial \dot{\hat{q}}_3^i} + \mathbf{F}_{1c} \cdot \frac{\partial \mathbf{v}_{sc}}{\partial \dot{\hat{q}}_3^i} + \mathbf{M}_{1p} \cdot \frac{\partial \boldsymbol{\omega}_{rp}}{\partial \dot{\hat{q}}_3^i} \\ &+ \mathbf{M}_{1c} \cdot \frac{\partial \boldsymbol{\omega}_{rc}}{\partial \dot{\hat{q}}_3^i} + \mathbf{F}_{2p} \cdot \frac{\partial \mathbf{v}_{ap}}{\partial \dot{\hat{q}}_3^i} + \mathbf{F}_{2c} \cdot \frac{\partial \mathbf{v}_{ac}}{\partial \dot{\hat{q}}_3^i} \\ &+ \mathbf{M}_{2p} \cdot \frac{\partial \boldsymbol{\omega}_{rp}}{\partial \dot{\hat{q}}_3^i} + \mathbf{M}_{2c} \cdot \frac{\partial \boldsymbol{\omega}_{rc}}{\partial \dot{\hat{q}}_3^i},\end{aligned} \tag{117}$$

where

$$[\hat{q}_3^i] = \begin{bmatrix} R & \phi & \theta & \gamma & x_{sp} & y_{sp} & \delta_p & x_{ac} & y_{ac} & \delta_{c2} & u_1 & u_2 & u_3 & u_4 & u_5 & u_6 & u_7 & u_8 \end{bmatrix}. \tag{118}$$

Similarly, the kinetic energy, $\hat{T}_3$, the potential energy, $\hat{U}_3$, and the Rayleigh dissipation function, $\hat{D}_3$, are given by

$$\begin{aligned}\hat{U}_3 =& m_m g \mathbf{x}_m \cdot \mathbf{E}_3 + m_b g \mathbf{x}_b \cdot \mathbf{E}_3 + m_r g \mathbf{x}_r \cdot \mathbf{E}_3 \\ &+ \frac{1}{2} k_m (R - R_0)^2 + \frac{1}{2} k_b \gamma^2 + \frac{1}{2} \sum_{j=1}^{4} \mathbf{u}_j \cdot \mathbf{K}_j \mathbf{u}_j,\end{aligned} \tag{119}$$

$$\begin{aligned}\hat{T}_3 =& \frac{1}{2} m_m \mathbf{v}_m \cdot \mathbf{v}_m + \frac{1}{2} m_b \mathbf{v}_b \cdot \mathbf{v}_b + \frac{1}{2} m_r \mathbf{v}_r \cdot \mathbf{v}_r \\ &+ \frac{1}{2} \boldsymbol{\omega}_b \cdot \mathbf{J}_b \boldsymbol{\omega}_b + \frac{1}{2} \boldsymbol{\omega}_r \cdot \mathbf{J}_r \boldsymbol{\omega}_r + \frac{1}{2} \sum_{j=1}^{4} \dot{\mathbf{u}}_j^t \cdot \mathbf{M}_j \dot{\mathbf{u}}_j^t,\end{aligned} \tag{120}$$

$$\hat{D}_3 = \frac{1}{2} c_m \dot{R}^2 + \frac{1}{2} c_b \dot{\gamma}^2 + \frac{1}{2} \sum_{j=1}^{4} \dot{\mathbf{u}}_j \cdot \mathbf{C}_j \dot{\mathbf{u}}_j. \tag{121}$$

In this case, we have $\mathbf{F}_{1p}$, $\mathbf{F}_{1c}$, $\mathbf{M}_{1p}$, $\mathbf{M}_{1c}$, $\mathbf{F}_{2p}$, $\mathbf{F}_{2c}$, $\mathbf{M}_{2p}$, and $\mathbf{M}_{2c}$, which all follow the same definitions as those from HS1 and HS2. The position vectors are defined as:

$$\mathbf{x}_g = u_{g1} \mathbf{E}_1 + u_{g2} \mathbf{E}_2, \tag{122}$$

$$\mathbf{x}_{sc} = 0.5(u_1 + u_5)\mathbf{E}_1 + 0.5(u_3 + u_7)\mathbf{E}_2 + \ell_q \mathbf{E}_3 + \mathbf{x}_g = x_{sc}\mathbf{E}_1 + y_{sc}\mathbf{E}_2 + \ell_q \mathbf{E}_3, \tag{123}$$

$$\mathbf{x}_{sp} = x_{sp}\mathbf{E}_1 + y_{sp}\mathbf{E}_2 + \ell_q \mathbf{E}_3, \tag{124}$$

$$\mathbf{x}_r = \ell_r \mathbf{E}_3 + \mathbf{x}_{sp}, \tag{125}$$

$$\mathbf{x}_{ap} = \ell_{ax} \mathbf{r}_{1p} + \ell_{az} \mathbf{E}_3 + \mathbf{x}_r, \tag{126}$$

$$\mathbf{x}_{ac} = x_{ac}\mathbf{E}_1 + y_{ac}\mathbf{E}_2 + (\ell_q + \ell_c + \ell_{az})\mathbf{E}_3, \tag{127}$$

$$\mathbf{x}_b = \ell_b \mathbf{b}_1 + \mathbf{x}_{ac}, \tag{128}$$

$$\mathbf{x}_t = \ell_t \mathbf{b}_1 + \mathbf{x}_b, \tag{129}$$

$$\mathbf{x}_m = R\mathbf{e}_R + \mathbf{x}_t, \tag{130}$$

$$\mathbf{u}_j = [u_{2j-1} \;\; u_{2j}]^T, \tag{131}$$

where Eqs. (122)-(131) all have the same physical meaning as their corresponding Eqs. (10)-(17), except that $\mathbf{x}_{sc}$ defines the position of the base of the crane cabin from the computational side and $\mathbf{x}_{sp}$ defines the position of the base of the crane cabin from the physical side and $\mathbf{x}_{ac}$ is the position of the connection point between the crane cabin and the boom from the computational side and $\mathbf{x}_{ap}$ is the position of the connection point between the crane cabin and the boom from the physical side. Also, the following quantities are defined as:

$$x_{sc} = 0.5(u_1 + u_5) + u_{g1},\ \ y_{sc} = 0.5(u_3 + u_7) + u_{g2}, \qquad (132)$$
$$\delta_c = 0.25\Big(\frac{u_1 - u_5}{l_x} + \frac{u_3 - u_7}{l_y}\Big).$$

The required vectors and rotation tensors are given by:

$$\mathbf{r}_{ip} = \mathbf{R}_{1p}\mathbf{E}_i, \qquad (133)$$

where $\mathbf{r}_{ip}$ is the co-rotational basis of the crane cabin from the physical side.

$$\mathbf{r}_{ic} = \mathbf{R}_{1c}\mathbf{E}_i, \qquad (134)$$

where $\mathbf{r}_{ic}$ is the co-rotational basis of the crane cabin from the computational side.

$$\mathbf{b}_i = \mathbf{R}_2\mathbf{r}_{ic}, \qquad (135)$$

where $\mathbf{b}_i$ is the co-rotational basis of the boom.

$$\mathbf{R}_{1p} = \begin{bmatrix} \cos(\alpha + \delta_p) & -\sin(\alpha + \delta_p) & 0 \\ \sin(\alpha + \delta_p) & \cos(\alpha + \delta_p) & 0 \\ 0 & 0 & 1 \end{bmatrix}_{\mathbf{E}_i \otimes \mathbf{E}_j} \qquad (136)$$

is the rotation tensor from the Cartesian basis to the $\mathbf{r}_{ip}$ basis.

$$\mathbf{R}_{1c} = \begin{bmatrix} \cos(\alpha + \delta_{c2}) & -\sin(\alpha + \delta_{c2}) & 0 \\ \sin(\alpha + \delta_{c2}) & \cos(\alpha + \delta_{c2}) & 0 \\ 0 & 0 & 1 \end{bmatrix}_{\mathbf{E}_i \otimes \mathbf{E}_j} \qquad (137)$$

is the rotation tensor from the Cartesian basis to the $\mathbf{r}_{ic}$ basis.

$$\mathbf{R}_2 = \begin{bmatrix} \cos(\beta + \gamma) & 0 & -\sin(\beta + \gamma) \\ 0 & 1 & 0 \\ \sin(\beta + \gamma) & 0 & \cos(\beta + \gamma) \end{bmatrix}_{\mathbf{r}_{ic} \otimes \mathbf{r}_{jc}} \qquad (138)$$

is the rotation tensor from the $\mathbf{r}_{ic}$ basis to the $\mathbf{b}_i$ basis.

$$\mathbf{e}_R = \cos(\theta)\sin(\phi)\mathbf{E}_1 + \cos(\phi)\mathbf{E}_2 - \sin(\theta)\sin(\phi)\mathbf{E}_3, \qquad (139)$$

$$\mathbf{e}_\phi = \cos(\theta)\cos(\phi)\mathbf{E}_1 - \sin(\phi)\mathbf{E}_2 - \sin(\theta)\cos(\phi)\mathbf{E}_3, \qquad (140)$$

and

$$\mathbf{e}_\theta = -\sin(\theta)\mathbf{E}_1 - \cos(\theta)\mathbf{E}_3, \qquad (141)$$

define the spherical basis vectors to define the position of the payload. Finally, the velocity vectors are as follows:

$$\mathbf{v}_g = \dot{u}_{g1}\mathbf{E}_1 + \dot{u}_{g2}\mathbf{E}_2, \qquad (142)$$

$$\mathbf{v}_{sc} = 0.5(\dot{u}_1 + \dot{u}_5)\mathbf{E}_1 + 0.5(\dot{u}_3 + \dot{u}_7)\mathbf{E}_2 + \mathbf{v}_g = \dot{x}_{sc}\mathbf{E}_1 + \dot{y}_{sc}\mathbf{E}_2, \qquad (143)$$

$$\mathbf{v}_{sp} = \dot{x}_{sp}\mathbf{E}_1 + \dot{y}_{sp}\mathbf{E}_2, \qquad (144)$$

$$\mathbf{v}_r = \mathbf{v}_{sp}, \qquad (145)$$

$$\mathbf{v}_{ap} = \ell_{ax}(\dot{\alpha} + \dot{\delta}_p)\mathbf{r}_{2p} + \mathbf{v}_r, \qquad (146)$$

$$\mathbf{v}_{ac} = \dot{x}_{ac}\mathbf{E}_1 + \dot{y}_{ac}\mathbf{E}_2, \qquad (147)$$

$$\mathbf{v}_b = \ell_b(\dot{\beta} + \dot{\gamma})\mathbf{b}_3 + \ell_b(\dot{\alpha} + \dot{\delta}_{c2})\cos(\beta + \gamma)\mathbf{r}_{2c} + \mathbf{v}_{ac}, \tag{148}$$

$$\mathbf{v}_t = \ell_t(\dot{\beta} + \dot{\gamma})\mathbf{b}_3 + \ell_t(\dot{\alpha} + \dot{\delta}_{c2})\cos(\beta + \gamma)\mathbf{r}_{2c} + \mathbf{v}_b, \tag{149}$$

$$\mathbf{v}_m = \dot{R}\mathbf{e}_R + R\dot{\theta}\mathbf{e}_\phi + R\sin(\phi)\dot{\theta}\mathbf{e}_\theta + \mathbf{v}_t, \tag{150}$$

$$\dot{\mathbf{u}}^t_j = [\dot{u}_{2j-1} \;\; \dot{u}_{2j}]^T - \begin{cases} [\dot{u}_{g1} \;\; \dot{u}_{g1}]^T \text{ if } j \text{ is odd} \\ [\dot{u}_{g2} \;\; \dot{u}_{g2}]^T \text{ if } j \text{ is even,} \end{cases} \tag{151}$$

where Eqs. (142)-(151) are the velocities of the corresponding positions from Eqs. (122)-(131). Also, we have the following angular velocity vectors:

$$\boldsymbol{\omega}_{rc} = (\dot{\alpha} + \dot{\delta}_{c2})\mathbf{E}_3, \tag{152}$$

which is the angular velocity of the crane cabin from the computational side.

$$\boldsymbol{\omega}_{rp} = (\dot{\alpha} + \dot{\delta}_p)\mathbf{E}_3, \tag{153}$$

which is the angular velocity of the crane cabin from the physical side.

$$\boldsymbol{\omega}_b = -(\dot{\beta} + \dot{\gamma})\mathbf{r}_{2c} + \boldsymbol{\omega}_{rc}, \tag{154}$$

which is the angular velocity of the boom.

In the ideal setting, we have

$$\mathbf{F}_{1c} \cdot \mathbf{E}_1 = -\mathbf{F}_{1p} \cdot \mathbf{E}_1, \;\; \mathbf{F}_{1c} \cdot \mathbf{E}_2 = -\mathbf{F}_{1p} \cdot \mathbf{E}_2, \;\; \mathbf{M}_{1c} \cdot \mathbf{E}_3 = -\mathbf{M}_{1p} \cdot \mathbf{E}_3. \tag{155}$$

and

$$\mathbf{F}_{2c} \cdot \mathbf{E}_1 = -\mathbf{F}_{2p} \cdot \mathbf{E}_1, \;\; \mathbf{F}_{2c} \cdot \mathbf{E}_2 = -\mathbf{F}_{2p} \cdot \mathbf{E}_2, \;\; \mathbf{M}_{2c} \cdot \mathbf{E}_3 = -\mathbf{M}_{2p} \cdot \mathbf{E}_3. \tag{156}$$

As was the case for HS1 and HS2, we still need more equations to properly solve for the motion of HS3. To do this we use the same error model described before: a spring-mass-damper system controlled by a PI controller. The equations for which are given by

$$\underline{D}_c[\hat{\mathbf{u}}_{c3}]\Big|_{\mathcal{I}_{c3}} = \underline{D}_p[\hat{\mathbf{u}}_{p3}]\Big|_{\mathcal{I}_{p3}}. \tag{157}$$

In this case $\hat{\mathbf{u}}_{c3}$ and $\hat{\mathbf{u}}_{p3}$ are given by

$$\hat{\mathbf{u}}_{c3} = \begin{bmatrix} x_{sc} & y_{sc} & \delta_c & x_{ac} & y_{ac} & \delta_{c2} \end{bmatrix}^T, \qquad \hat{\mathbf{u}}_{p3} = \begin{bmatrix} x_{sp} & y_{sp} & \delta_p & x_{ap} & y_{ap} & \delta_{p2} \end{bmatrix}^T, \tag{158}$$

where the operators $\underline{D}_c[\hat{\mathbf{u}}_{c3}]$ and $\underline{D}_p[\hat{\mathbf{u}}_{p3}]$ have the following definitions:

$$\underline{D}_c[\hat{\mathbf{u}}_{c3}] = \Big(k_a k_i + (k_a k_p + c_a k_i)\frac{d}{dt} + c_a k_p \frac{d^2}{dt^2}\Big)\hat{\mathbf{u}}_{c3}, \tag{159}$$

and

$$\underline{D}_p[\hat{\mathbf{u}}_{p3}] = \Big(k_a k_i + (k_a(1 + k_p) + c_a k_i)\frac{d}{dt} + (c_a(1 + k_p))\frac{d^2}{dt^2} + m_a \frac{d^3}{dt^3}\Big)\hat{\mathbf{u}}_{p3}, \tag{160}$$

where the parameters are the same as those mentioned for HS1. The system is subject to the following constraints

$$x_{ap} = x_{sp} + l_{ax}\cos(\alpha + \delta_p), \;\; y_{ap} = y_{sp} + l_{ax}\sin(\alpha + \delta_p), \;\; \delta_p = \delta_{p2}, \tag{161}$$

in order to maintain rigid body motion for the cabin. All of the previous equations give the necessary equations to solve for the motion of HS3.

4. Analysis

For the analysis of the crane structure, all of the physical dimensions defined in the previous section need to be defined, along with a set of initial conditions for time integration. See Appendix A for all of the physical data, initial conditions, and other constants. Note that all values represent non-dimensionlized values. The majority of the analysis consists of evaluating how a harmonic displacement applied at the base of the structure affects the hybrid responses of the three different hybrid systems. To accomplish this we define u_{g2} as

$$u_{g2} = A\cos(\Omega t), \tag{162}$$

where A is the amplitude of the displacement and Ω is the angular frequency of the displacement. We set $A = 0.1$ and vary Ω from 0.1 to 10 with a step size of 0.05. Throughout the analysis, the L^2 norm [27] is used to evaluate the error. There are three different types of L^2 errors that are used in this paper:

1. Whole System Error: when both reference system and hybrid system have equivalent quantities to compare.

$$E^{WS}_{\bullet}(t) = \frac{\sqrt{\int_0^t ||\mathbf{a}_{\bullet} - \hat{\mathbf{a}}_{\bullet}||^2}}{\sqrt{\int_0^t ||\mathbf{a}_{\bullet}||^2}}, \tag{163}$$

   where $\mathbf{a}_{\bullet}$ and $\hat{\mathbf{a}}_{\bullet}$ are the state vectors for the reference and hybrid systems respectively for some physical quantities represented by $\bullet$. And $||\bullet||$ is the standard 2-norm of a vector.

2. Hybrid Interface Error: when the hybrid system has equivalent quantities on the $\mathcal{C}$-side and $\mathcal{P}$-side that both need to be compared to the reference system.

$$E^{HI}_{\bullet}(t) = \frac{\sqrt{\int_0^t ||\mathbf{a}_{\bullet} - \hat{\mathbf{a}}_{c\bullet}||^2 + ||\mathbf{a}_{\bullet} - \hat{\mathbf{a}}_{p\bullet}||^2}}{\sqrt{\int_0^t ||\mathbf{a}_{\bullet}||^2}}, \tag{164}$$

   where $\mathbf{a}_{\bullet}$, $\hat{\mathbf{a}}_{c\bullet}$, and $\hat{\mathbf{a}}_{p\bullet}$ are state vectors of the reference, computational side, and physical side, respectively, for some quantity represented by $\bullet$.

3. Hybrid System Error: the error between equivalent quantities on the $\mathcal{C}$-side and $\mathcal{P}$-side, which is the error at the hybrid interfaces.

$$E^{HS}_{\bullet}(t) = \frac{\sqrt{\int_0^t ||\hat{\mathbf{a}}_{c\bullet} - \hat{\mathbf{a}}_{p\bullet}||^2}}{\sqrt{\int_0^t ||\hat{\mathbf{a}}_{c\bullet}||^2}}, \tag{165}$$

   where $\hat{\mathbf{a}}_{c\bullet}$, and $\hat{\mathbf{a}}_{p\bullet}$ are state vectors of the computational side and physical side, respectively, for some quantity represented by $\bullet$. Note, this type of error is not dependent upon the reference system.

Note, that in all three cases, the error is normalized, in the first two cases, to the reference system, and for the third case, to the $\mathcal{C}$-side. Whole system errors are computed for the states of the system ($\mathbf{a}_s$, $\hat{\mathbf{a}}_s$) and the total energy of the system ($\mathbf{a}_E$, $\hat{\mathbf{a}}_E$). Hybrid interface errors and hybrid system errors are computed for δ ($\mathbf{a}_\delta$, $\hat{\mathbf{a}}_{c\delta}$, $\hat{\mathbf{a}}_{p\delta}$), x_s ($\mathbf{a}_x$, $\hat{\mathbf{a}}_{cx}$, $\hat{\mathbf{a}}_{px}$), and y_s ($\mathbf{a}_y$, $\hat{\mathbf{a}}_{cy}$, $\hat{\mathbf{a}}_{py}$). See Appendix B for definitions of all of the previously mentioned vectors. In order to let all of the L^2 errors approach a steady-state value, the L^2 errors for the following figures are all computed out to a value of $t = 1000$.

Figures 8-15 show all of the L^2 errors for the different properties mentioned earlier. From examining these figures, we see fairly smooth curves for the all of the L^2 errors except around $\Omega = 1.75$ and $\Omega = 5.4$. First, the analysis ignores the areas around $\Omega = 1.75$ and $\Omega = 5.4$, and analysis of the cause and impact of those two regions comes afterward.

4.1. Comparing the Reference System to the Hybrid Systems

While excluding the regions around $\Omega = 1.75$ and $\Omega = 5.4$, we notice that the errors tend to be the smallest towards $\Omega = 0$, and get larger as $\Omega = 10$. This makes sense because, as the frequency is increased, it is harder for

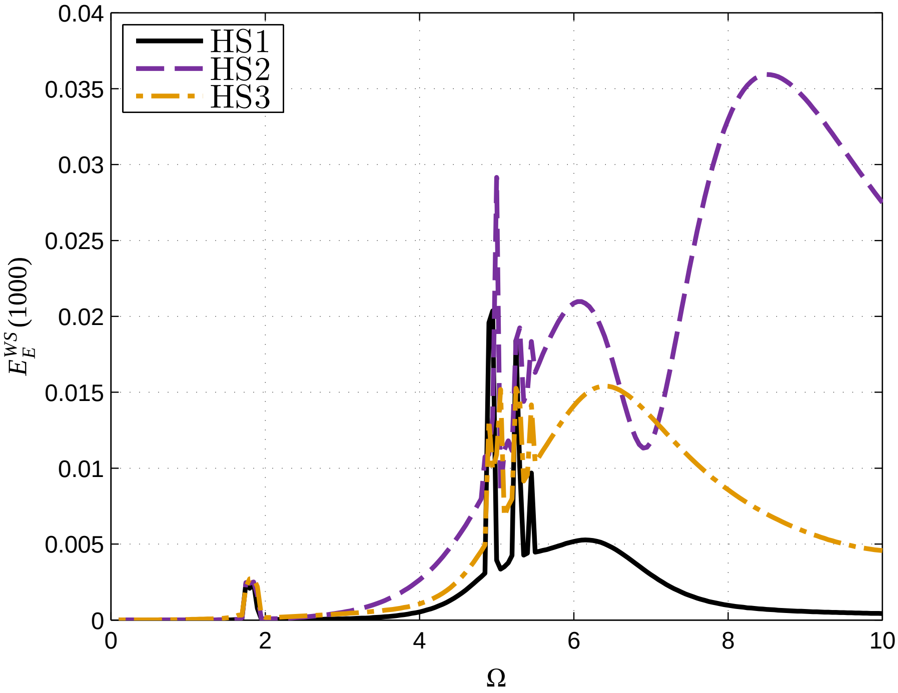

Figure 8: The Whole System Error of the total energy for all three hybrid systems as a function of Ω.

the controller to maintain dynamic matching between both the $\mathcal{C}$-side and $\mathcal{P}$-side, which leads to larger errors. This effect is clearly shown in Figs. 13 and 14, which shows that the error between equivalent quantities on the $\mathcal{C}$-side and $\mathcal{P}$-side are approximately growing with Ω. We note that in some cases the L^2 error goes above 1, which is over 100% error, for example HS2 in Fig. 9, which indicates poor matching between the reference and hybrid systems. However, by examining Fig. 8, we see that – even for higher frequencies – the error for HS2 never goes above 0.04, or 4%. This is interesting in that the states are not matching very well between the two systems, however, the total energy of the two systems is matching fairly well. This result is similar to one found by Drazin and Govindjee [17], indicating that different aspects of hybrid simulation can be accurate, while others can be inaccurate. This leads to a question of what is desired from hybrid simulation, and what can one reasonable expect from a hybrid simulation response. From comparing Figs. 8 and 9, we can see that the errors for all three systems are typically much smaller for E_E^{WS} than for E_s^{WS}. Since the E_s^{WS} represents how well the entire motion of the hybrid system matches that of the reference system, it is clear that the total energy of the system matches better than the actual motion of the system. Thus, even though it may seem like the hybrid simulation is not representative of the true dynamics – especially for the case of HS2 when E_s^{WS} goes above 1 – it can still provide accurate results for other physical properties of the system, in this case the total energy. This reinforces the conclusion that to fully utilize hybrid simulation, sometimes it is beneficial to look at as many physical quantities as possible, because the actual motion may not be as accurate as one would like to believe.

4.2. Comparing the Hybrid Systems to Each Other

From examining Figs. 8-15, it is clear that HS1, HS2, and HS3 all have unique error responses for all of the properties shown. This indicates that the location of the hybrid split affects the results produced from a hybrid simulation. For example, all of the L^2 errors for HS1 never goes above 0.4, whereas HS3 typically has a larger L^2 error than HS1, yet never goes above 0.7, and HS2 typically has the largest error, and in many cases goes above 1. From these results it seems that, on average, HS1 provides the best results, followed by HS3, and HS2 is the worst. This may be somewhat surprising, in that HS3 has two hybrid splits, whereas HS2 only has one, and one might expect

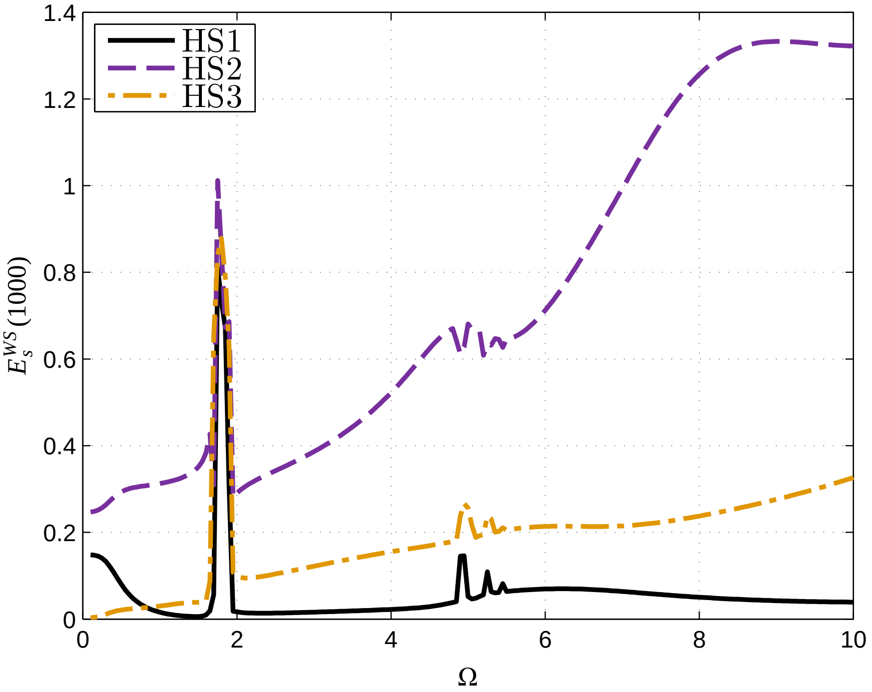

Figure 9: The Whole System Error of the states for all three hybrid systems as a function of Ω.

that having only one hybrid split would imply that there is less chance for error to be introduced into the system. However, the results show that more hybrid splits does not directly correlate to more error in the hybrid system. This implies that there are *good* and *bad* locations to create a hybrid split, where a *good* hybrid split location will be one that minimizes error introduced into the hybrid system, and a *bad* hybrid split location is one that will cause the error in the system to rise quickly. For instance, HS1 is the best hybrid system since it has the least amount of error in all three of our error metrics. This indicates that it has a *good* hybrid split location, or a hybrid split location that does not alter the system dynamics a great deal. Similarly, HS2 is the worst hybrid system, since it has the most error in all three of our error metrics. This indicates that it has a *bad* hybrid split location, or a split location that drastically changes the system dynamics. Since HS3 has the both split locations (the ones used by HS1 and HS2), it indicates that HS3 should have both a *good* and *bad* hybrid split location. Since HS3 is in between HS1 and HS2, when it comes to L^2 errors, it might indicate that *good* and *bad* locations have an averaging effect.

4.3. Analyzing the Frequency Response

From Figs. 8-15, we see fairly smooth curves for the all of the L^2 errors except around $\Omega = 1.75$ and $\Omega = 5.4$, which have what seem to be random spikes in the error. To try to better understand the error spikes, we look at the frequency response of the unforced system ($u_{gy} = 0$). The frequency responses for all four systems are shown in Fig. 16, where we can see that there are frequency peaks around $\Omega = 1.75$ and $\Omega = 5.4$. This indicates that resonant frequencies of the system are causing the spikes in the L^2 error curves. These error spikes are similar to the error spikes found by Drazin et. al. [15] and Bakhaty et. al. [16], which were typically located near resonant frequencies of the system. Due to the appearance of error spikes in simple linear systems with constant error, as well as in this paper with a nonlinear multi-degree of freedom system with basic PI controller, it seems to imply that error spikes near resonant frequencies are a fundamental aspect of hybrid simulation. This makes it clear that hybrid simulation has a hard time dealing with the resonant frequencies of a system, and one should be aware of this and try to avoid exciting the resonant frequencies when administering a hybrid simulation experiment in order to avoid any unnecessary error.

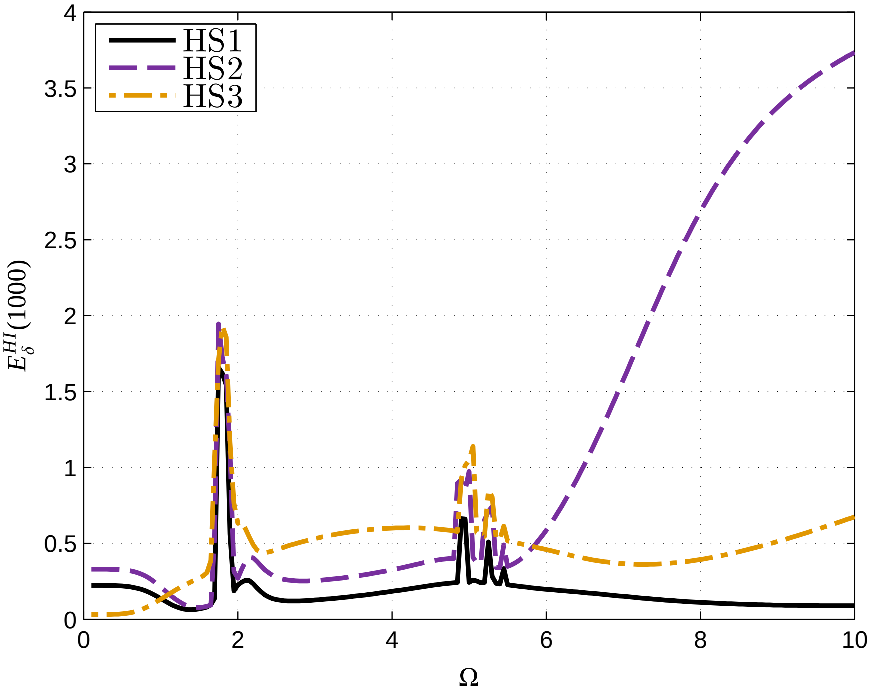

Figure 10: The Hybrid Interface Error of δ for all three hybrid systems as a function of Ω.

However, it worth noting that all four systems have nearly identical frequency responses, as seen in Fig. 16, which indicates that the hybrid split did not change the frequency response of the system, and leaves the resonant frequencies intact. This can be an invaluable resource, in that, one can use the hybrid system to determine the resonant frequencies without actually having the reference system.

4.4. Discussion

In the previous section, we analyzed different aspects of a theoretical hybrid simulation setup. While we were able to find situations in which the results of a hybrid test were comparable to that of the reference test, there were numerous occasions in which the hybrid results did not match the reference system. This indicates that the use of hybrid simulation to effectively test different mechanical systems and structures is not guaranteed, but rather requires careful consideration of how the hybrid system is constructed. As we have seen, it is possible for something as simple as the location of the hybrid split to drastically change the outcome of a hybrid test. We have also seen that certain physical properties match fairly well, while other properties do not match at all. However, all of this was determined with knowledge of the reference system. In an actual hybrid experiment, the reference system response most likely will not be known, which would make it impossible to calculate errors similar to those in this paper. For this reason, a hybrid experiment needs to be well thought out beforehand to make sure that all error inducing situations are reduced as much as possible. In addition, a hybrid test should look at as many physical quantities as possible, such as displacements, velocities, energies, frequencies, etc., because this will give the user a greater chance at receiving useful and accurate data. If possible, it seems advisable to conduct as many hybrid tests as possible for a single mechanical system. By doing this, there will then be multiple sets of data that can be compared to see if there is any correlation between the sets of data, which would potentially point in the direction of the reference response. Finally, with more data from multiple hybrid tests, it will provide possible ranges of motion that the mechanical system will experience; in essence creating bounds on the motion that will be useful for designing systems or structures that utilize the core component of original hybrid test.

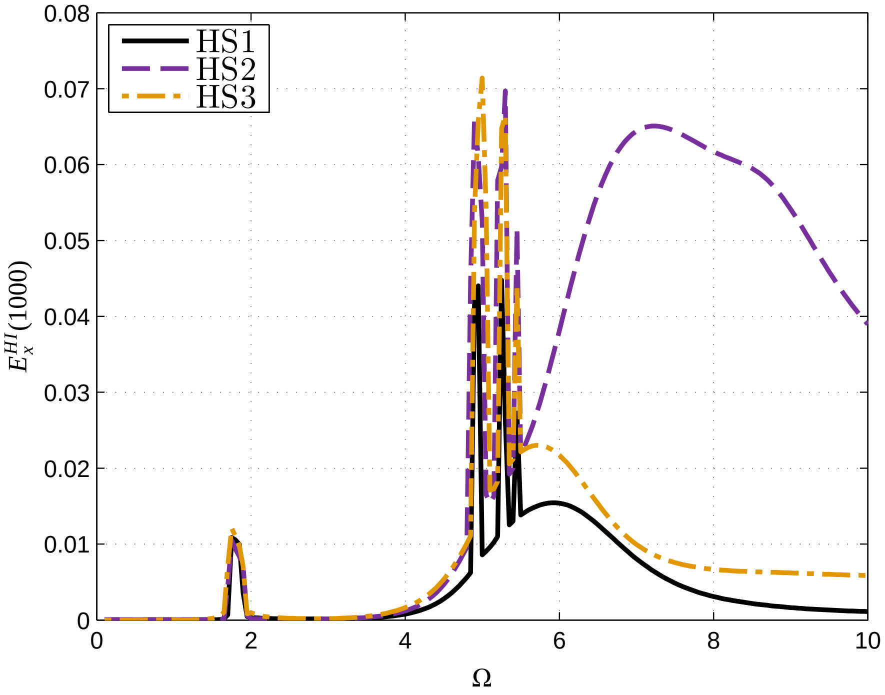

Figure 11: The Hybrid Interface Error of x_s for all three hybrid systems as a function of Ω.

5. Conclusion

This paper aimed to expand upon the theoretical knowledge of hybrid simulation. It utilized a best case scenario for errors that might occur in a hybrid simulation experiment, namely systematic magnitude and phase mismatch at the hybrid interface through the application of a PI controller. While this is by no means a comprehensive list of all possible errors that might occur, it gives us a good starting point. This paper tested an multi-degree of freedom, nonlinear, crane structure with a theoretical hybrid simulation setup developed previously [15, 16]. From this setup, we devised three different hybrid systems: one with the split between the cabin and supporting structure, one with the split between the cabin and the boom, and one with both hybrid splits. In this way we were not only able to compare the hybrid system to the reference system, but we were also able to compare the effectiveness of the hybrid systems to each other. In previous works, it was found that hybrid simulation can produce accurate results, but those were done with very simple linear or single degree of freedom nonlinear systems. This paper explored the effects of how hybrid simulation scales with the size and complexity of the structure. While analyzing the hybrid systems, we found many correlations to previous works, such as the error spikes in the frequency domains [15, 16], as well as the fact that certain dynamical properties can be accurately described by a hybrid test while others can not [17]. This shows that the results and analysis from even the simple systems maintains its relevancy, even for more complicated structures. From comparing the hybrid systems to each other, we found that the location of the hybrid splits, as well as how many hybrid splits there are, can have a significant impact on the overall results. This makes it critical that one fully understands the situation in which they are conducting a hybrid test. Thus, overall we can see that hybrid simulation can be quite effective if used properly and if proper care is taken when setting up the actual hybrid test.

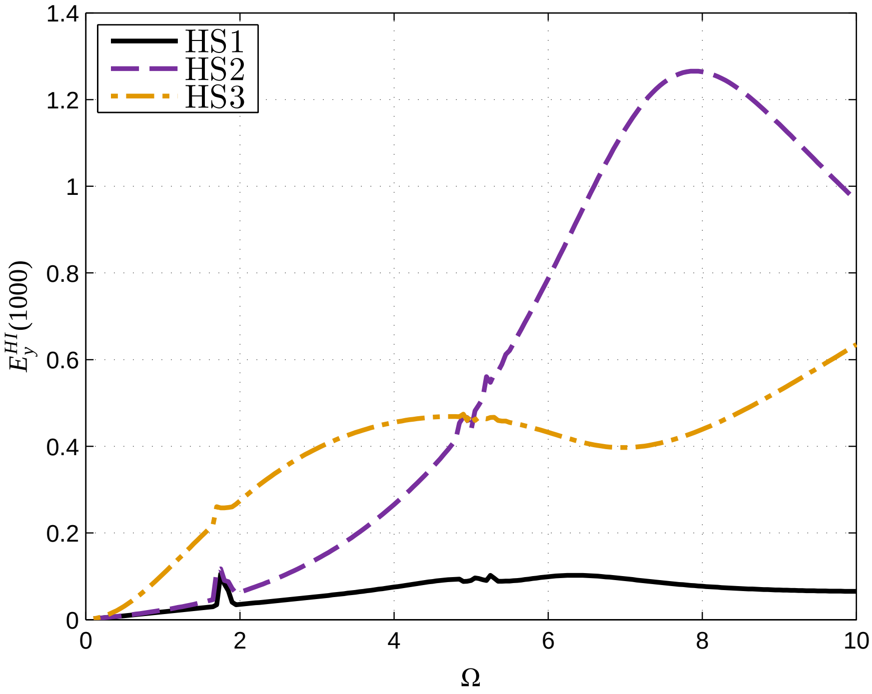

Figure 12: The Hybrid Interface Error of y_s for all three hybrid systems as a function of Ω.

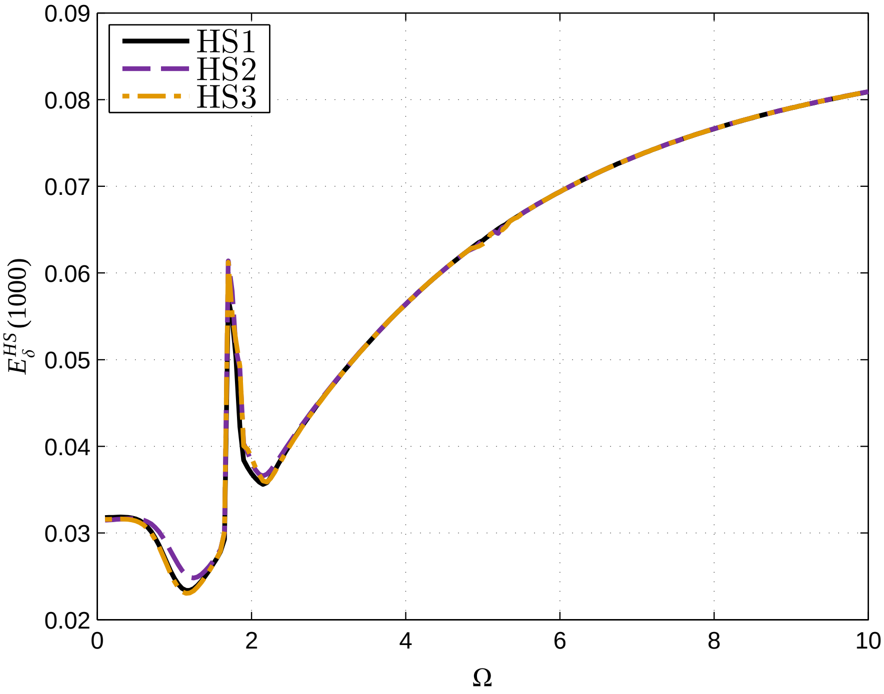

Figure 13: The Hybrid System Error of δ for all three hybrid systems as a function of Ω.

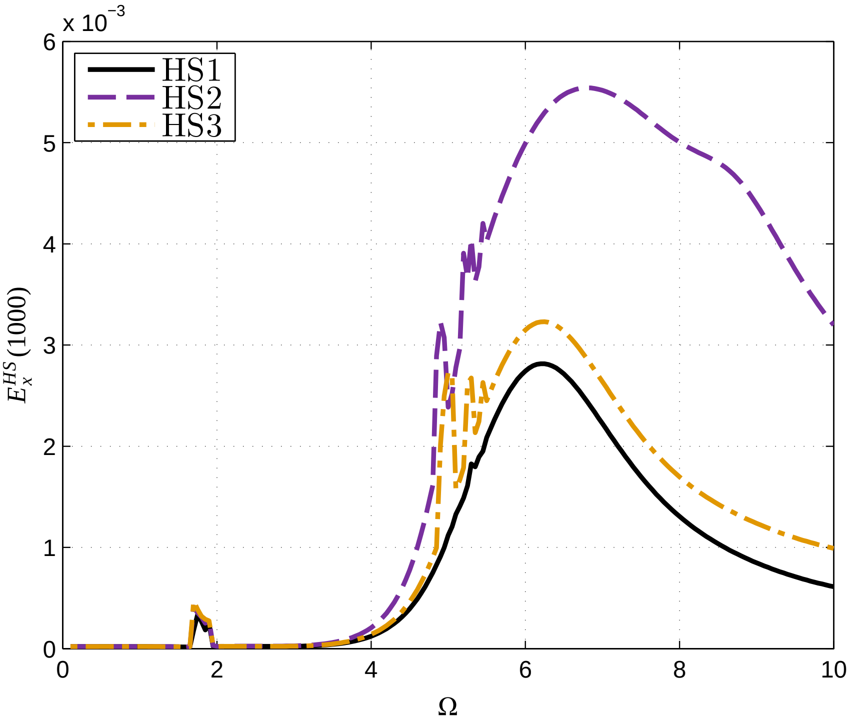

Figure 14: The Hybrid System Error of x_s for all three hybrid systems as a function of Ω.

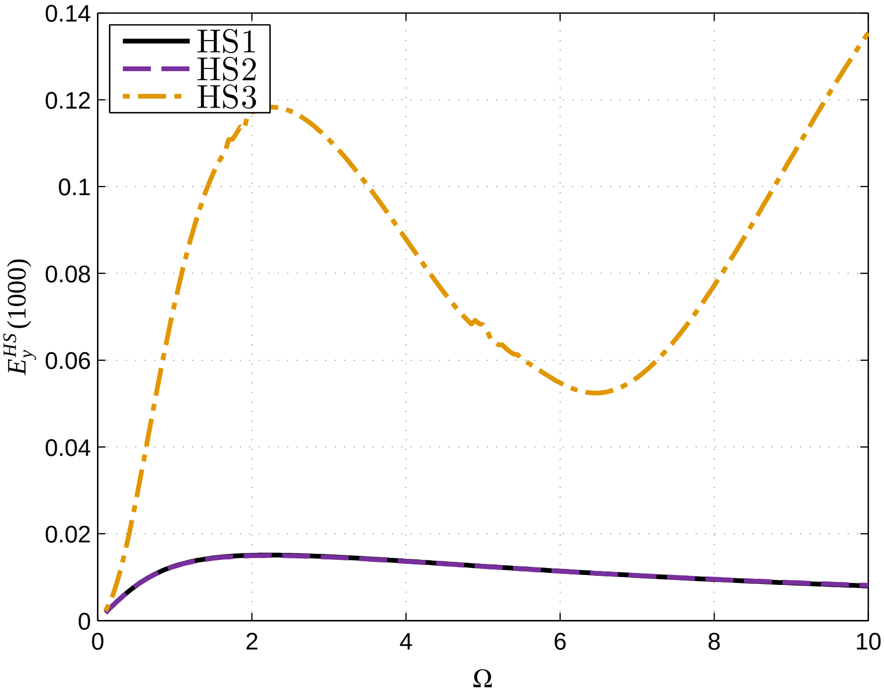

Figure 15: The Hybrid System Error of y_s for all three hybrid systems as a function of Ω.

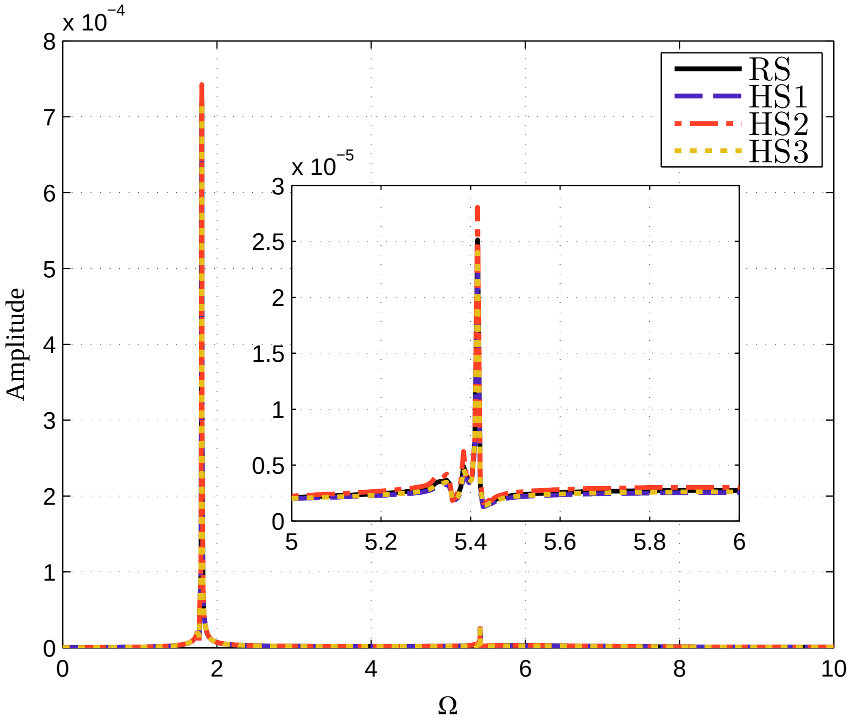

Figure 16: Frequency response of the unforced system. The insert is a zoomed in section around the peak near $\Omega = 5.4$.

References

[1] K. Takanashi, M. Nakashima, Japanese activities on on-line testing, Journal of Engineering Mechanics 113 (7) (1987) 1014–1032.
[2] P. S. B. Shing, S. A. Mahin, Pseudodynamic test method for seismic performance evaluation: theory and implementation., Tech. Rep. UCB-EERC-84-01, Earthquake Engineering Research Center, Berkeley, CA (1984).
[3] P. S. B. Shing, S. A. Mahin, Elimination of spurious higher-mode response in pseudodynamic tests, Earthquake Engineering and Structural Dynamics 15 (4) (1987) 409–424.
[4] O. S. Bursi, C. Jia, L. Vulcan, S. A. Neild, D. J. Wagg, Rosenbrock-based algorithms and subcycling strategies for real-time nonlinear substructure testing, Earthquake Engineering and Structural Dynamics 40 (1) (2011) 1–19.
[5] K. M. Mosalam, S. Günay, Seismic performance evaluation of high voltage disconnect switches using real-time hybrid simulation: I. system development and validation, Earthquake Engineering and Structural Dynamics 43 (8) (2014) 1205–1222.
[6] S. Günay, K. M. Mosalam, Seismic performance evaluation of high voltage disconnect switches using real-time hybrid simulation: II. parametric study, Earthquake Engineering and Structural Dynamics 43 (8) (2014) 1223–1237.
[7] C. Chen, J. M. Ricles, T. L. Karavasilis, Y. Chae, R. Sause, Evaluation of a real-time hybrid simulation system for performance evaluation of structures with rate dependent devices subjected to seismic loading, Engineering Structures 35 (2012) 71 – 82.
[8] X. Gao, N. Castaneda, S. Dyke, Experimental validation of a generalized procedure for mdof real-time hybrid simulation, Journal of Engineering Mechanics 140 (4) (2014) 04013006.
[9] B. Dong, R. Sause, J. Ricles, Accurate real-time hybrid earthquake simulations on large-scale mdof steel structure with nonlinear viscous dampers, Earthquake Engineering and Structural Dynamics 44 (12) (2015) 2035–2055.
[10] E-defense, http://www.bosai.go.jp/hyogo/ehyogo/profile/introduction/Introduction.html, [Online; accessed 08-June-2016].
[11] A. H. Schellenberg, Advanced implementation of hybrid simulation, Ph.D. thesis, University of California, Berkeley, CA (2008).
[12] A. P. Darby, A. Blakeborough, M. S. Williams, Improved control algorithm for real-time substructure testing, Earthquake Engineering and Structural Dynamics 30 (3) (2001) 431–448.
[13] D. Wagg, S. Neild, P. Gawthrop, Real-Time Testing With Dynamic Substructuring, Springer Vienna, Vienna, 2008, pp. 293–342.
[14] C. Chen, J. M. Ricles, Tracking error-based servohydraulic actuator adaptive compensation for real-time hybrid simulation, Journal of Structural Engineering 136 (4) (2010) 432–440.
[15] P. L. Drazin, S. Govindjee, K. M. Mosalam, Hybrid simulation theory for continuous beams, ASCE Journal of Engineering Mechanics 141 (7) (2015) 04015005.
[16] A. A. Bakhaty, S. Govindjee, K. M. Mosalam, Theoretical evaluation of hybrid simulation applied to continuous plate structures), Journal of Engineering Mechanics 142 (12) (2016) 04016093.
[17] P. L. Drazin, S. Govindjee, Hybrid simulation theory for a classical nonlinear dynamical system, Journal of Sound and Vibration 392 (2017) 240 – 259.
[18] S. N. Voormeeren, D. de Klerk, D. J. Rixen, Uncertainty quantification in experimental frequency based substructuring, Mechanical Systems and Signal Processing 24 (1) (2010) 106–118.
[19] M. Ahmadizadeh, G. Mosqueda, A. M. Reinhorn, Compensation of actuator delay and dynamics for real time hybrid structural simulation, Earthquake Engineering and Structural Dynamics 37 (1) (2008) 21–42.
[20] W. Lau, K. Low, Motion analysis of a suspended mass attached to a crane, Computers & Structures 52 (1) (1994) 169 – 178.
[21] B. Posiadaa, Influence of crane support system on motion of the lifted load, Mechanism and Machine Theory 32 (1) (1997) 9 – 20.
[22] B. Jerman, P. Podraj, J. Kramar, An investigation of slewing-crane dynamics during slewing motiondevelopment and verification of a mathematical model, International Journal of Mechanical Sciences 46 (5) (2004) 729 – 750.
[23] O. M. O'Reilly, Intermediate Dynamics for Engineers, Cambridge University Press, New York, 2008.
[24] S. S. Rao, Mechanical Vibrations, Prentice Hall, Upper Saddle River, NJ, 2004.
[25] A. K. Chopra, Dynamics of Structures: Theory and applications to earthquake engineering, Prentice Hall., Upper Saddle River, NJ, 2004.
[26] N. S. Nise, Control Systems Engineering, John Wiley & Sons, New York, 2008.
[27] C. Johnson, Numerical Solution of Partial Differential Equations by the Finite Element Method, Dover Publications, Mineola, NY, 2009.

Appendix A. Physical Data

The following tables provide all of the numerical values used throughout this paper, along with $g = 9.8$. All values were chosen in an attempt to approximate a scaled down crane structure and are considered dimensionless. Note, for the initial conditions used for time integration, all non-zero values are shown in Table A.5, with the exception of u_{g2}, whose definition is provided within the paper.

ℓ_x	ℓ_y	ℓ_s	ℓ_r	ℓ_{ax}	ℓ_{az}	ℓ_b	ℓ_t	R_0
0.25	0.25	3	0.75	0.05	0.05	1	1	3

Table A.1: All lengths used for the crane systems.

$\mathbf{M}_j$	m_r	m_b	m_m	$\mathbf{J}_r$	$\mathbf{J}_b$
$\begin{bmatrix} 9.36 & 0 \\ 0 & 18.72 \end{bmatrix}_{\mathbf{E}_i \otimes \mathbf{E}_j}$	19.5	3.9	0.78	$\begin{bmatrix} 4.0625 & 0 & 0 \\ 0 & 4.0625 & 0 \\ 0 & 0 & 0.8125 \end{bmatrix}_{\mathbf{r}_i \otimes \mathbf{r}_j}$	$\begin{bmatrix} 0.0016 & 0 & 0 \\ 0 & 1.308 & 0 \\ 0 & 0 & 1.308 \end{bmatrix}_{\mathbf{b}_i \otimes \mathbf{b}_j}$

Table A.2: All masses and inertias used for the crane systems.

$\mathbf{K}_j$	k_b	k_m	$\mathbf{C}_j$	c_b	c_m
$\begin{bmatrix} 2023.3 & -2201.5 \\ -2201.5 & 4562.5 \end{bmatrix}_{\mathbf{E}_i \otimes \mathbf{E}_j}$	2.6×10^6	4.19×10^7	$\begin{bmatrix} 39.96 & -0.02 \\ -0.02 & 79.93 \end{bmatrix}_{\mathbf{E}_i \otimes \mathbf{E}_j}$	191.21	342.96

Table A.3: All stiffnesses and damping constants used for the crane systems.

m_a	c_a	k_a	k_p	k_i
1	156.5	245.25	10	55

Table A.4: All constants used for hybrid control.

R	ϕ	θ	α	β	u_{gx}
3	1.47	1.47	0.25	0.5	1

Table A.5: All non-zero initial conditions.

Appendix B. Error State Vectors

Let $\mathbf{a}_d$ be the vector of displacements, then

$$\mathbf{a}_d = \begin{bmatrix} R & \phi & \theta & \gamma & u_1 & u_2 & u_3 & u_4 & u_5 & u_6 & u_7 & u_8 \end{bmatrix}^T, \tag{B.1}$$

and equivalently for $\hat{\mathbf{a}}_d$, where all the quantities in Eq. (B.1) have the same meaning as in Section 3.1. And let $\mathbf{a}_v = \dot{\hat{\mathbf{a}}}_d$, where the superposed dot $(\dot{\ })$indicates a time derivative of the given quantity. Then,

$$\mathbf{a}_s = \begin{bmatrix} \mathbf{a}_d & \mathbf{a}_v \end{bmatrix}^T, \tag{B.2}$$

Similarly for $\hat{\mathbf{a}}_s$. Then, for the total energy vectors, we have

$$\mathbf{a}_E = \begin{bmatrix} E \end{bmatrix}, \tag{B.3}$$

where $E = T + U$. See Section 3.1 for definitions of T and U. And equivalently for $\hat{\mathbf{a}}_E$. Finally, the vectors for δ, x, and y, are given by

$$\mathbf{a}_\delta = \begin{bmatrix}\delta & \dot{\delta}\end{bmatrix}^T, \ \hat{\mathbf{a}}_{c\delta} = \begin{bmatrix}\delta_c & \dot{\delta}_c\end{bmatrix}^T, \ \hat{\mathbf{a}}_{p\delta} = \begin{bmatrix}\delta_p & \dot{\delta}_p\end{bmatrix}^T, \tag{B.4}$$

$$\mathbf{a}_x = \begin{bmatrix}x_s & \dot{x}_s\end{bmatrix}^T, \ \hat{\mathbf{a}}_{cx} = \begin{bmatrix}x_{sc} & \dot{x}_{sc}\end{bmatrix}^T, \ \hat{\mathbf{a}}_{px} = \begin{bmatrix}x_{sp} & \dot{x}_{sp}\end{bmatrix}^T, \tag{B.5}$$

$$\mathbf{a}_y = \begin{bmatrix}y_s & \dot{y}_s\end{bmatrix}^T, \ \hat{\mathbf{a}}_{cy} = \begin{bmatrix}y_{sc} & \dot{y}_{sc}\end{bmatrix}^T, \ \hat{\mathbf{a}}_{py} = \begin{bmatrix}y_{sp} & \dot{y}_{sp}\end{bmatrix}^T, \tag{B.6}$$

where x_s, y_s, and δ are the $\mathbf{E}_1$ position, the $\mathbf{E}_2$ position, and rotation angle of the crane cabin for the reference system, x_{sc}, y_{sc}, and δ_c are the $\mathbf{E}_1$ position, the $\mathbf{E}_2$ position, and rotation angle of the crane cabin for the hybrid systems from the computational side, and x_{sp}, y_{sp}, and δ_p are the $\mathbf{E}_1$ position, the $\mathbf{E}_2$ position, and rotation angle of the crane cabin for the hybrid systems from the physical side.